

## ARTICLE



# A unique hyperdynamic dimer interface permits small molecule perturbation of the melanoma oncoprotein MITF for melanoma therapy

Zaizhou Liu<sup>1,12</sup>, Kaige Chen<sup>2,9,12</sup>, Jun Dai<sup>3,4</sup>, Peng Xu<sup>1,5</sup>, Wei Sun<sup>6</sup>, Wanlin Liu<sup>6</sup>, Zhixin Zhao<sup>1</sup>, Steven P. Bennett<sup>7</sup>, Peifeng Li<sup>1</sup>, Tiancheng Ma<sup>1</sup>, Yuqi Lin<sup>1</sup>, Akinori Kawakami<sup>3</sup>, Jing Yu<sup>1</sup>, Fei Wang<sup>1</sup>, Chunxi Wang<sup>1</sup>, Miao Li<sup>1</sup>, Peter Chase<sup>7,10</sup>, Peter Hodder<sup>7,11</sup>, Timothy P. Spicer<sup>7</sup>, Louis Scampavia<sup>7</sup>, Chunyang Cao<sup>1</sup>, Lifeng Pan<sup>1,5</sup>, Jiajia Dong<sup>1</sup>, Yong Chen<sup>6</sup>, Biao Yu<sup>1,5</sup>, Min Guo<sup>1,8</sup>, Pengfei Fang<sup>1,5</sup>, David E. Fisher<sup>3</sup> and Jing Wang<sup>1</sup>

© The Author(s) under exclusive licence to Center for Excellence in Molecular Cell Science, Chinese Academy of Sciences 2022

**Microphthalmia transcription factor (MITF)** regulates melanocyte development and is the “lineage-specific survival” oncogene of melanoma. MITF is essential for melanoma initiation, progression, and relapse and has been considered an important therapeutic target; however, direct inhibition of MITF through small molecules is considered impossible, due to the absence of a ligand-binding pocket for drug design. Here, our structural analyses show that the structure of MITF is hyperdynamic because of its out-of-register leucine zipper with a 3-residue insertion. The dynamic MITF is highly vulnerable to dimer-disrupting mutations, as we observed that MITF loss-of-function mutations in human Waardenburg syndrome type 2A are frequently located on the dimer interface and disrupt the dimer forming ability accordingly. These observations suggest a unique opportunity to inhibit MITF with small molecules capable of disrupting the MITF dimer. From a high throughput screening against 654,650 compounds, we discovered compound TT-012, which specifically binds to dynamic MITF and destroys the latter’s dimer formation and DNA-binding ability. Using chromatin immunoprecipitation assay and RNA sequencing, we showed that TT-012 inhibits the transcriptional activity of MITF in B16F10 melanoma cells. In addition, TT-012 inhibits the growth of high-MITF melanoma cells, and inhibits the tumor growth and metastasis with tolerable toxicity to liver and immune cells in animal models. Together, this study demonstrates a unique hyperdynamic dimer interface in melanoma oncoprotein MITF, and reveals a novel approach to therapeutically suppress MITF activity.

*Cell Research* (2023) 33:55–70; <https://doi.org/10.1038/s41422-022-00744-5>

## INTRODUCTION

Malignant melanoma is an aggressive and treatment-resistant human cancer that arises from melanocytes, which synthesize melanin and are responsible for skin color.<sup>1</sup> The treatment resistance of melanoma is considered to be predominantly related to the special resistance of melanocytes to environmental exposure-induced apoptosis and senescence.<sup>1–5</sup> Genes that control melanocyte cell cycle progression and differentiation also play crucial roles in melanoma.

Microphthalmia transcription factor (MITF) is the master regulator of melanocytes. It governs the expression of genes that are critical for pigment synthesis, melanocyte cell cycle progression and differentiation.<sup>6–8</sup> MITF is also a lineage-specific survival

oncogene in malignant melanoma.<sup>9</sup> Amplified MITF has been found in ~20% of melanomas and MITF<sup>E318K</sup> mutation occurred at a significantly higher frequency in patients with genetic predisposition to develop melanoma.<sup>9–11</sup> Re-expression of MITF has been found in relapsed melanoma patients and drives resistance to MAPK pathway inhibition.<sup>12–14</sup> In melanoma, low levels of MITF generate G1-arrested, invasive, senescent cells, while cells expressing MITF either proliferate or differentiate.<sup>15–17</sup> The oncogenic feature of MITF largely results from its vital role in melanocyte survival and migration through regulating genes including *BCL2*, *c-Met*, *CDK2*, *p16/Ink4*, and *p21*.<sup>2,18–21</sup>

Introducing dominant-negative *MITF* (DN-MITF) into human melanoma cell lines inhibited cell proliferation and enhanced

<sup>1</sup>State Key Laboratory of Bioorganic and Natural Products Chemistry, Center for Excellence in Molecular Synthesis, Shanghai Institute of Organic Chemistry, University of Chinese Academy of Sciences, Chinese Academy of Sciences, Shanghai, China. <sup>2</sup>School of Biomedical Sciences and Engineering, South China University of Technology, Guangzhou International Campus, Guangzhou, Guangdong, China. <sup>3</sup>Department of Dermatology, Cutaneous Biology Research Center, Mass. General Hospital, Harvard Medical School, Boston, MA, USA. <sup>4</sup>School of Pharmacy, University of Wisconsin-Madison, Madison, WI, USA. <sup>5</sup>School of Chemistry and Materials Science, Hangzhou Institute for Advanced Study, University of Chinese Academy of Sciences, Hangzhou, Zhejiang, China. <sup>6</sup>Department of Musculoskeletal Oncology, Fudan University Shanghai Cancer Center; Department of Oncology, Shanghai Medical College, Fudan University, Shanghai, China. <sup>7</sup>Scripps Research, Jupiter, FL, USA. <sup>8</sup>Kangma-Healthcode Biotech Co., Ltd., Shanghai, China. <sup>9</sup>Present address: School of Life Sciences, University of Science and Technology of China, Hefei, Anhui, China. <sup>10</sup>Present address: BMS Inc., Lawrenceville, NJ, USA. <sup>11</sup>Present address: Amgen Inc., Thousand Oaks, CA, USA. <sup>12</sup>These authors contributed equally: Zaizhou Liu, Kaige Chen. <sup>✉</sup>email: chenyong@fudan.edu.cn; byu@sioc.ac.cn; guomin@healthcodon.com; fangpengfei@sioc.ac.cn; DFISHER3@mgh.harvard.edu; Jwang@sioc.ac.cn

Received: 16 August 2021 Accepted: 17 October 2022

Published online: 2 January 2023

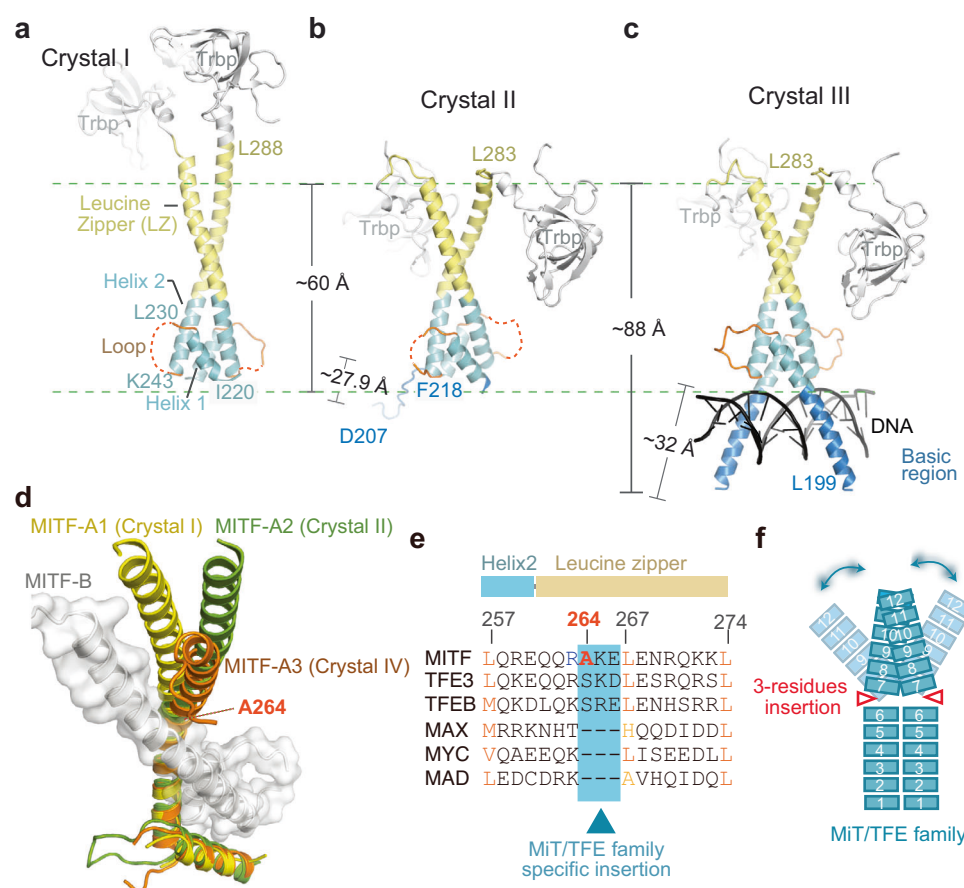


**Fig. 1** MITF has a distinct dynamic leucine zipper. **a–c** Overall crystal structures of MITF HLH-LZ region (**a**, Crystal I), bHLH-LZ domain (**b**, Crystal II), and bHLH-LZ domain complexed with E-box DNA (**c**, Crystal III). Without DNA, two MITF chains form a dimer with disordered basic region. Each chain contains two continuous helices linked by the loop region, and the LZ (yellow) is traceable in all three structures. The basic region (Leu199 to Phe218) folds into a helix upon binding to DNA, extending helix 1 (H1) (**c**). **d** Superimposition of Crystal I, Crystal II, and Crystal IV by using one subunit of the MITF dimer as the reference (designated as MITF-B) shows that the LZ regions of the other subunit (designated as MITF-A) vary greatly. The separation point is the residue Ala264. **e** Sequence alignment between the MiT/TFE family and MYC family transcription factors. Compared with MYC family proteins, the MiT/TFE family members have three additional residues in the first heptad repeat of the LZ. Residue Ala264 is located in this heptad and represents the first residue of the three residues <sup>264</sup>AKE<sub>266</sub>. **f** Schematic interpretation of the 3-residue insertion causing dynamic LZ in the MiT/TFE family.

sensitivity to chemotherapeutic agents.<sup>9</sup> Knocking down *MITF* could enhance the overall cytotoxicity of BRAF inhibitors.<sup>14</sup> And knocking down the upstream regulator *TYRO3* suppressed *MITF* expression and further inhibited tumorigenesis in a mouse model.<sup>22</sup> Suppression of USP13, the deubiquitination enzyme that stabilizes MITF protein, led to loss of MITF protein and inhibited melanoma growth in vitro and in a mouse model.<sup>23</sup> Reduction of the MITF protein level through shRNA or a histone deacetylase (HDAC) inhibitor blunted the cAMP-mediated resistance to MAPK pathway inhibitors.<sup>12</sup> Together, accumulating evidence shows that MITF is an important therapeutic target for melanoma. However, no pharmacological approach has been available to directly target MITF due to the absence of a ligand-binding pocket or groove interface within MITF for drug design.

Most of the human melanocyte MITF structure is predicted to be disordered, except for a conserved basic helix-loop-helix-leucine zipper (bHLH-LZ) domain (Supplementary information, Fig. S1). The HLH-LZ region promotes the dimerization of MITF and the basic region forms helix and directly binds the E-box (CANNTG) or M-box (CATGTG) DNA located on the promoters of MITF target genes.<sup>24,25</sup> Removal of the LZ region disrupted the DNA-binding ability of MITF in vitro.<sup>26</sup> In addition, MITF has a marked kink in one of the two LZ helices which is necessary to limit heterodimerization, because removal of the kink-associated

three residues permits MITF to dimerize with MAX, another transcription factor of a different bHLH-LZ family.<sup>25,27</sup> MITF loss-of-function mutations found in human patients with Waardenburg syndromes type 2 A (WS2A) and Tietz syndromes (TS) and other vertebrate models, are frequently located in the HLH-LZ region, which also indicates that this region plays a key role in the function of MITF. Interestingly, the HLH-LZ region has no direct interaction with DNA, but mutations in it could disrupt the MITF–DNA interaction in an electrophoretic mobility shift (EMSA) assay.<sup>28–31</sup> The mechanisms underlying these observations are not fully understood.

Here, through a combination of structural and biochemical analyses, we elucidate that the structure of MITF is hyperdynamic and highly vulnerable to dimer-disrupting mutations. In addition, we identified a potent small-molecule MITF dimer disruptor TT-012, revealing a novel approach to directly inhibit MITF which has great potential to benefit melanoma treatment.

## RESULTS

### MITF crystal structures with traceable LZ

The integrity of the LZ region is important for the physiological function of MITF.<sup>26</sup> However, most part of the LZ region was not traceable in previous complex structures of MITF and E-box or

M-box DNA (PDB codes: 4ATI and 4ATK).<sup>25</sup> To understand how the LZ region affects DNA binding, we fused Trbp111, a scaffold protein from the thermophilic bacterial *Aquifex aeolicus* to the C-terminus of the bHLH-LZ domain of human MITF (isoform M1, residues 199–288, denoted as MITF<sub>bHLH-LZ</sub>), to reduce the potential flexibility and facilitate crystallization. This fusion protein (MITF<sub>bHLH-LZ</sub>-Trbp111) has similar M-box DNA binding ability to MITF<sub>bHLH-LZ</sub> itself, indicating that the Trbp111 fusion does not interfere with MITF–DNA interaction (Supplementary information, Fig. S2). The structure of the HLH-LZ domain (residues 217–288) without the basic region was first determined by K<sub>2</sub>PtBr<sub>6</sub>-based single wavelength anomalous diffraction to a resolution of 3.0 Å, denoted as Crystal I (Fig. 1a; Supplementary information, Table S1 and Fig. S3a–c). The first helix started from Ile220 and ended at Leu230 (Helix 1, Fig. 1a). Residues Lys243 to Leu288 formed an extended second helix that constituted of Helix 2 and the following LZ (Fig. 1a).

Using the molecular replacement method with the Crystal I as a searching model, we then determined the structures of the complete bHLH-LZ domain (residues 199–288) in apo form to a resolution of 2.3 Å (Crystal II, Fig. 1b) and the bHLH-LZ domain in complex with E-box DNA to a resolution of 3.2 Å (Crystal III, Fig. 1c) (Supplementary information, Table S1 and Fig. S3d–i). Without DNA, the basic region (residues 199–218) was disordered and could be only partially traced as a 12-residue loop in one of the MITF molecules (from Asp207 to Phe218, Fig. 1b). In the presence of E-box DNA, the basic region folded into a helix extending by ~32 Å to bind the major groove of the duplex DNA, and the LZ region was observed to contribute to the dimerization (Fig. 1c).

#### Hyperdynamic feature of MITF

When we aligned Crystal I, Crystal II, Crystal III, and the previously reported mouse MITF apo structure (PDB code: 4ATH, here was denoted as Crystal IV),<sup>25</sup> the LZ regions above Ala264 showed different locations, implying its dynamic characteristics (Fig. 1d; Supplementary information, Fig. S4a). Even in one crystal unit, rotations between the two MITF dimers were observed (Supplementary information, Fig. S4b). In addition, while most part of LZ is not traceable in the complex structure of MITF with E-box or M-box DNA, the remaining observable LZ exhibited different conformations.<sup>25</sup> These observations suggest that the LZ region is dynamic and “flexible”, explaining the untraceable LZ in previous MITF–DNA crystals (PDB codes: 4ATI and 4ATK), as in these structures, the crystal packing is formed mainly by the bHLH and DNA and does not involve LZ, leaving the LZ un-restrained (Supplementary information, Fig. S5). By fusing the Trbp111 tag to the LZ of MITF to reduce its dynamics, we were able to capture the LZ in multiple different conformations in crystal structures.

The dynamic structural phenotype of MITF is not observed in the MYC/MAX/MAD family members which all contain a bHLH-LZ domain.<sup>32</sup> Based on the reported MYC-MAX (PDB code: 1NKP), MAD-MAX (PDB code: 1NLW) and MAX-MAX (PDB code: 1AN2) crystal structures,<sup>33</sup> all those dimers closely resemble each other and bind target DNA with structurally stable LZ (Supplementary information, Fig. S6a–c). According to the sequence alignment between MiT/TFE family and MYC/MAX/MAD family members, a 3-residue insertion beginning at the Ala264 bifurcation point in MITF<sub>(264AKE266)</sub> was found to be unique in the MiT/TFE family (Fig. 1e). The leucine zipper is classically characterized by heptad repeats of leucine residues over the alpha helix;<sup>34</sup> thus, this 3-residue insertion can interfere with the pairing and cause hyperdynamics of the LZs (Fig. 1f).

To experimentally confirm that the dynamics of MITF LZ is caused by the 3-residue insertion and not by the Trbp111 fusion during crystallization, we performed more biophysical analyses without the fusion tag. Removing the 3-residue insertion significantly increased the thermal stability of MITF\_WT (the bHLH-LZ domain of human MITF). The melting temperature (Tm)

of MITF<sub>Δ3</sub> (the bHLH-LZ domain with 3-residue insertion (264–266) removed) is 9.1 °C higher than that of MITF\_WT (41.4 °C vs 32.3 °C) by circular dichroism spectra analysis (Supplementary information, Fig. S6d), demonstrating that the 3-residue insertion affects the stability of the MITF dimer. In addition, despite the high thermostability of MITF\_WT when bound to DNA, removal of the 3-residue insertion can further increase its Tm by about 1 °C ( $P = 0.0038$ ), supporting the intrinsic dynamic property of the LZ region beyond DNA recognition (Supplementary information, Fig. S6e). Of note, the essential feature of a leucine zipper is the periodic repetition of leucine residues at every seventh position. Thus, insertion of 3 residues between L257 and L267 would tend to disturb the heptad repeat leucine of the leucine zipper. Indeed, removing <sup>259</sup>REQ<sub>261</sub> in MITF in the previous study also was shown to increase the thermostability of MITF,<sup>27</sup> suggesting that the key to the flexibility of the LZ is the insertion of 3 residues itself, rather than the chemistry of these residues.

We then designed a quantitative fluorescence anisotropy assay to monitor the dimerization of MITF using 5-iodoacetamido-Fluorescein (5-IAF)-labeled MITF, and the result showed that removal of the 3 residues can significantly increase the MITF dimer formation by ~24-fold (from 29.8 nM to 1.2 nM) (Supplementary information, Fig. S6f). In addition, we solved the crystal structure of MITF<sub>Δ3</sub> (Supplementary information, Table S1 and Fig. S3g, h), and observed a symmetric dimer that was more like a member of the MYC/MAX/MAD family (Supplementary information, Fig. S6i, j).

Together, these results suggest that the 3-residue insertion forced the out-of-register pairing of LZs and induced the dynamic characteristics of MITF.

#### MITF is susceptible to dimer-disturbing mutations

Nine of the 24 investigated MITF mutations in WS2A and TS are located in the HLH-LZ region (Fig. 2a, b; Supplementary information, Table S2). Among them, mutations I224S, S250P, Y253C, R259Stop, and N278D were shown to disrupt the MITF–DNA interaction in an electrophoretic mobility shift (EMSA) assay.<sup>31</sup> To quantify the effect of the mutations, we performed real-time kinetic binding experiments with M-box DNA labeled on the sensor (Supplementary information, Fig. S7a). Wild-type MITF interacts with M-box DNA in a kinetic process with  $k_{on} = 3.6E4 \pm 2.3E3$  (M·s)<sup>-1</sup>,  $k_{off} = 4.1E-3 \pm 2.9E-5$  s<sup>-1</sup> and  $K_d$  of 113 nM (Fig. 2c). Basic region mutations Del217R and R217I led to significant loss of DNA-binding ability (Supplementary information, Fig. S7b, c), and N210K mutant almost maintained the DNA-binding ability ( $K_d = 185$  nM, Supplementary information, Fig. S7d). We also examined the loss-of-function mutations H209R and I212N found in mice, and observed that they led to a 2.7-fold and a 8.9-fold decrease in DNA-binding activity, respectively (Supplementary information, Fig. S7e, f).

Then, we tested the HLH-LZ domain mutations, including I224S, S250P, Y253C, R259Stop, and N278D, all of which led to complete loss of DNA-binding ability (Fig. 2d–h). Moreover, I224S and N278D mutations reduced the transcriptional activity by 5–10-fold, while S250P and R259Stop mutants showed no transcriptional activity in a luciferase reporter assay in HEK293T cells (Fig. 2i). Therefore, through these quantitative analyses, we confirmed that mutations in the HLH-LZ region resulted in major damage to the function of MITF, even greater than those caused by some mutations in the basic region.

The five tested HLH-LZ region mutations (I224S, S250P, Y253C, R259Stop, and N278D) are located on the dimer interface in the MITF structure (Fig. 3a, b). Three other untested pathogenic mutations (269FS, 275FS, and 278FS) are frame-shift (FS) mutations that should cause great alterations to the LZ (Fig. 2a, b). Therefore, the loss of function effect of these mutations might be achieved by reducing the dimerization of MITF. To verify this, we examined the ability of MITF mutants to dimerize with wild type protein (MITF\_WT) by using pull-down assays, as the pathogenic

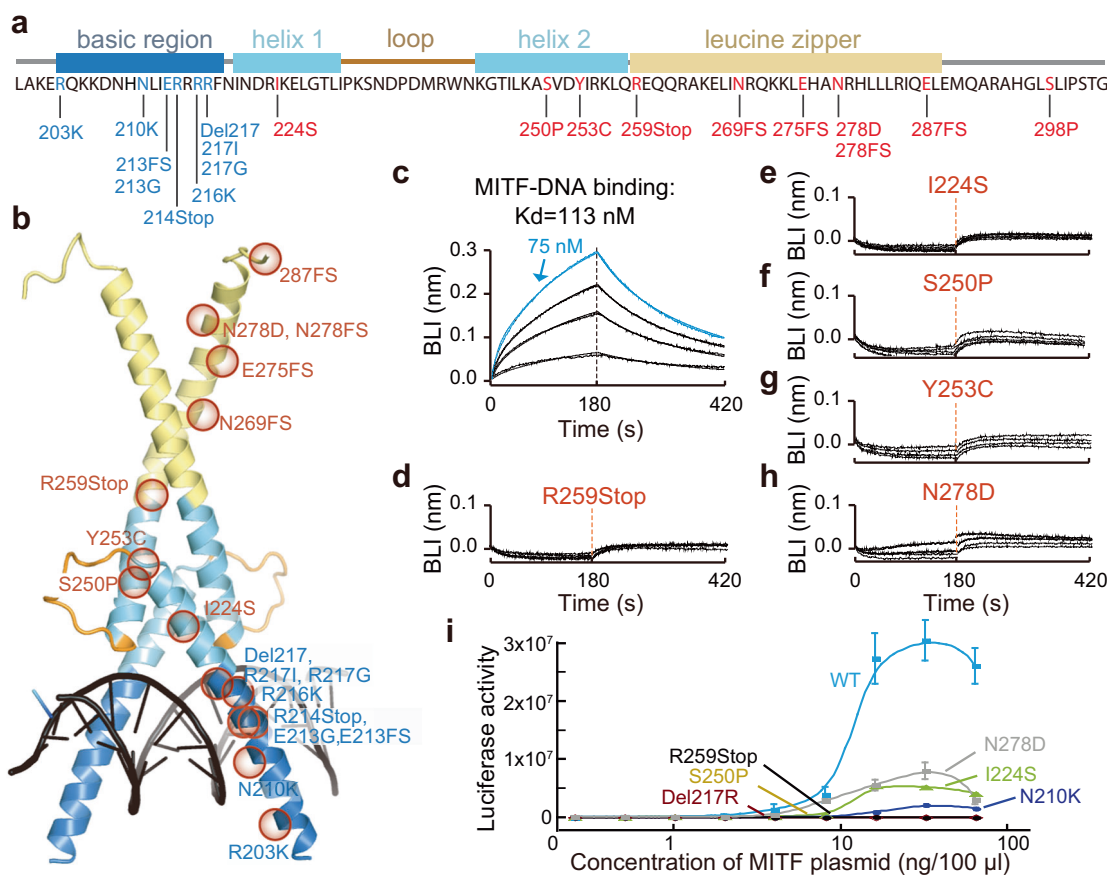


**Fig. 2 MITF loss-of-function mutations reveal the critical role of the HLH-LZ region. a, b** Locations of the WS2A- and TS-associated loss-of-function mutations in the bHLH-LZ region of MITF are indicated in the amino acid sequence (**a**) and the structure of the MITF bHLH-LZ domain (**b**, Crystal III). Except for the mutations within the DNA-binding site (the basic region), 9 mutations are located in the HLH-LZ region. **c** Real-time kinetic assays determining the DNA-binding ability of MITF. Wild-type MITF binds to the M-box DNA on the chip with  $k_{on} = 3.6E4 \pm 2.3E3$  (M·s) $^{-1}$ ,  $k_{off} = 4.1E3 \pm 2.9E-5$  s $^{-1}$  and  $K_d = 113$  nM. **d–h** Real-time kinetic assays determining the DNA-binding ability of MITF with different mutation in the HLH-LZ region, including R259Stop, I224S, S250P, Y253C, and N278D. These mutations completely lost their DNA binding ability. **i** TRPM1-Luc reporter assays showing that MITF mutants that lose DNA binding ability are defective in transcription in HEK293T cells. Error bars represent the SDs of three repeats.

mutations usually occurred in heterozygous form (Fig. 3c). Indeed, these mutations in HLH-LZ completely disrupted MITF dimer formation, while mutations in the basic region did not affect dimer formation (Fig. 3c). The fluorescence anisotropy assay further confirmed that MITF mutants with mutations in the basic region (Del217R and N210K) formed a dimer similar to the MITF\_WT dimer, while mutations in the HLH-LZ region (I224S, S250P, Y253C, R259Stop, and N278D) decreased the MITF-MITF dimerization affinities by over 500-fold (Fig. 3d).

To assess whether MITF is sensitive to subtle disruptions of the dimer interface, we designed three new mutations (L281K, L281R, and L281A). The residue Leu281 formed a hydrophobic interaction at the C-terminus end of the LZ region (Fig. 3b). Hence, the mutations of this residue were expected to yield the least secondary structural perturbations. Pull-down assays showed that the L281K and L281R mutations, which introduced a repulsive clash, substantially reduced MITF dimerization (Fig. 3c). Interestingly, the MITF dimer interface includes more interactions than those of the MAX dimer (Supplementary information, Fig. S8a-d); however, the Tm of the HLH-LZ region of MITF is over 23 °C lower than that of MAX (Supplementary information, Fig. S8d).<sup>35</sup> In the fluorescence anisotropy assay, while the L281A mutant showed a decreased dimerization affinity with MITF\_WT by over 1015-fold with a  $K_d$  above 40 μM (Supplementary information, Fig. S8e), a similar mutation on MAX (L95A) only reduced the MAX dimerization by 13.5-fold with a  $K_d$  of 177.3 nM (Supplementary

information, Fig. S8f), implying that the hyperdynamic and vulnerable nature of MITF is unique. Consistently, all three mutated MITF (L281A/K/R) lost the DNA binding ability (Fig. 3e). Moreover, when overexpressed in HEK293T cells, these mutants reduced the maximal transcriptional activity by 5–15-fold compared to MITF\_WT in the luciferase reporter assay (Fig. 3f).

Together, these results indicate that the hyperdynamic MITF is vulnerable to dimer disruption by single mutations in the HLH-LZ region (Fig. 3g). This finding also suggests that disrupting MITF dimer formation through small molecular compounds may be an effective method to suppress MITF activity.

#### High-throughput screening identifies a MITF dimer-breaking compound TT-012

To screen for small-molecule compounds that can disrupt MITF dimerization, we developed a fluorescence-based high-throughput AlphaScreen assay (MITF dimerization-based AlphaScreen, MIDAS) based on the dimerization of MITF proteins (Fig. 4a).<sup>36</sup> Using point mutations, we confirmed that the MIDAS assay was sensitive and specific to the dimerization of MITF. For example, mutations in the basic region, such as H209R and N210K, produced similar Alpha signals to those of the WT, indicating an undisturbed MITF dimer (Supplementary information, Fig. S9a, b). Disruption of dimerization using mutations such as I224S, S250P, Y253C, and N278D in the HLH-LZ region, produced a weakened Alpha signal (Supplementary information, Fig. S9c). Thus, the

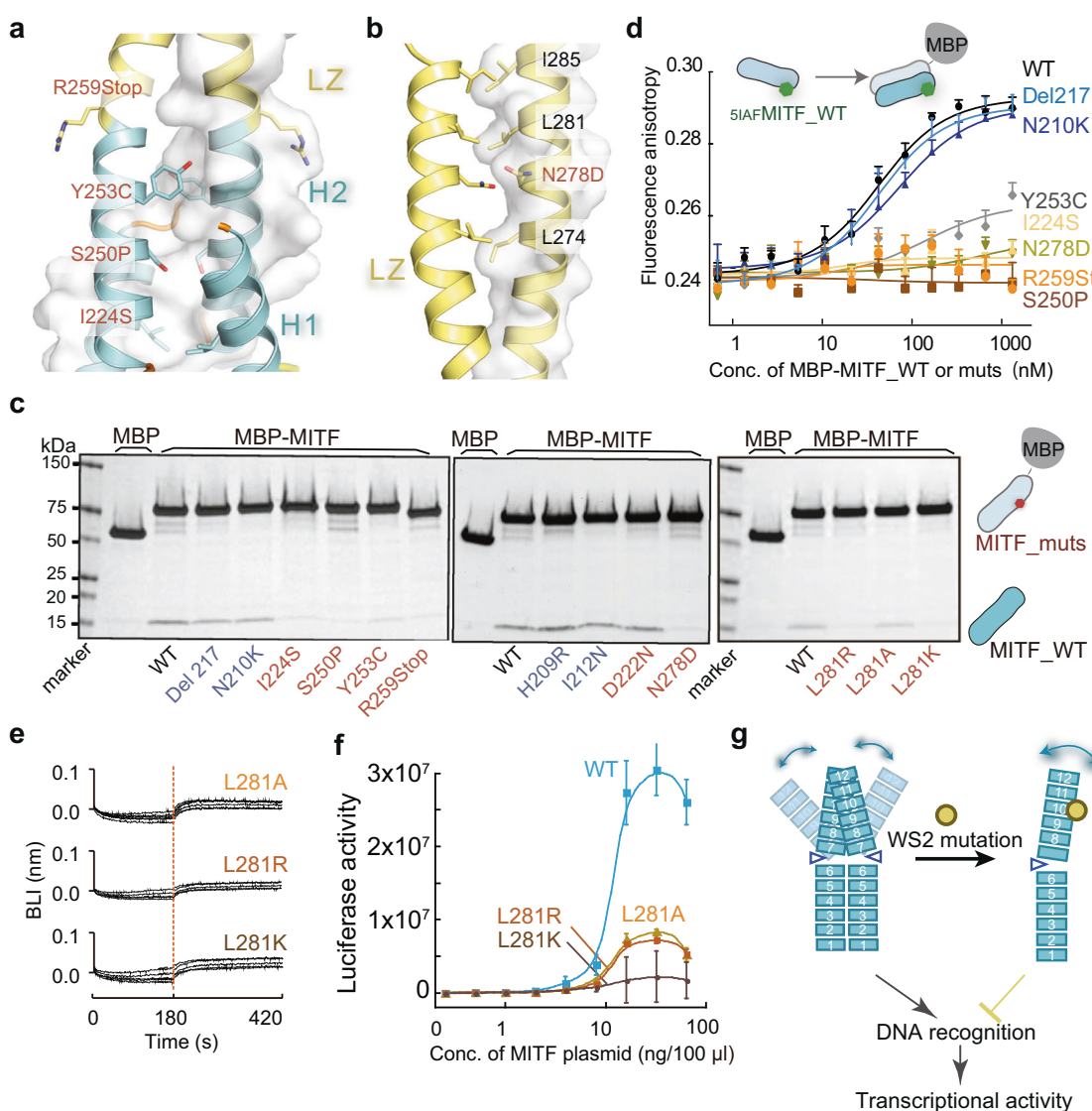


**Fig. 3** Loss-of-function mutations in HLH-LZ disrupt MITF dimer formation. **a, b** Loss-of-function mutations in the HLH-LZ region are located in the dimer interface of MITF. **c** Dimerization of MITF\_WT with mutants was assessed by pull-down assay. The MBP-MITF\_WT or MBP-MITF\_muts (MW 55 kDa) were used to pull down MITF\_WT (MW 15 kDa) at a concentration of 300 μM. Proteins were analyzed using Coomassie Brilliant Blue. Mutations in the HLH-LZ region and the basic region are labeled in red and blue, respectively. **d** Fluorescence anisotropy titration quantifies the MITF dimer affinity. MBP-MITF\_WT or mutants with gradient concentrations were titrated to <sup>5</sup>I<sub>A</sub>F-MITF\_WT with overnight incubation. MITF\_WT formed a dimer with a  $K_d$  of  $\sim 30 \pm 7.4$  nM. The mutants I224S, R259Stop, S250P, and N278D had no detectable signal for dimerization. Y253C showed a  $K_d$  of 1086 nM, 30 times weaker than WT. Mutants in the basic region (N210K, Del217R) showed similar binding ability to WT, with  $K_d$  values of 58 nM and 30 nM, respectively. **e** Real-time kinetic assays of the L281A/K/R mutants binding to M-box DNA. All three mutants had a strongly reduced DNA binding ability. **f** *TrpM1*-Luciferase reporter assay showing that the L281A/K/R mutants were defective in transcription in HEK293 cells. Error bars represent the SDs of three repeats. **g** Schematic cartoon showing that the intermolecular dynamic feature renders MITF susceptible to internal dimer disruption.

MIDAS assay could reflect the dimerization state of MITF, and was a practicable approach to screen MITF dimerization-disrupting compounds.

In total, we screened 654,650 compounds by using the MIDAS assay. TT-012, a small compound with a symmetric structure composed of furan and pyridine, was discovered as an effective MITF dimerization disruptor (Fig. 4b). The chemical and physical properties of TT-012 are shown in Supplementary information, Table S3. The  $IC_{50}$  of TT-012 in diminishing the Alpha signal generated by MITF dimer formation is 13.1 nM (Fig. 4c). In contrast, TT-012 had no effect on the Alpha signal generated by the interaction between lysyl-tRNA synthetase (LysRS) and aminoacyl-tRNA synthetase complex-interacting multifunctional protein 2 (AIMP2) which was established as a control (Fig. 4c).

To evaluate the cellular effect of TT-012 on MITF, we performed immunoprecipitation (IP) analysis on B16F10 cells expressing 3x Flag-tagged MITF<sub>bHLH-LZ</sub> using anti-Flag antibody. The results showed that TT-012 dose-dependently disrupted the interaction between Flag-MITF<sub>bHLH-LZ</sub> and the endogenous MITF, indicating that TT-012 attenuates the dimerization of bHLH-LZ from the two components (Fig. 4d). From this IP-Western assay, we deduced that TT-012 disrupted the MITF dimerization in 30–60 min (Supplementary information, Fig. S10). To further check the effect of TT-012 on endogenous MITF dimerization, we performed size exclusion chromatography (SEC) analysis on the lysates of B16F10 cell that were treated with TT-012 or DMSO, and observed that the proportion of monomer form of MITF significantly increased after TT-012 treatment (Fig. 4e). In the cross-linking assay, TT-012

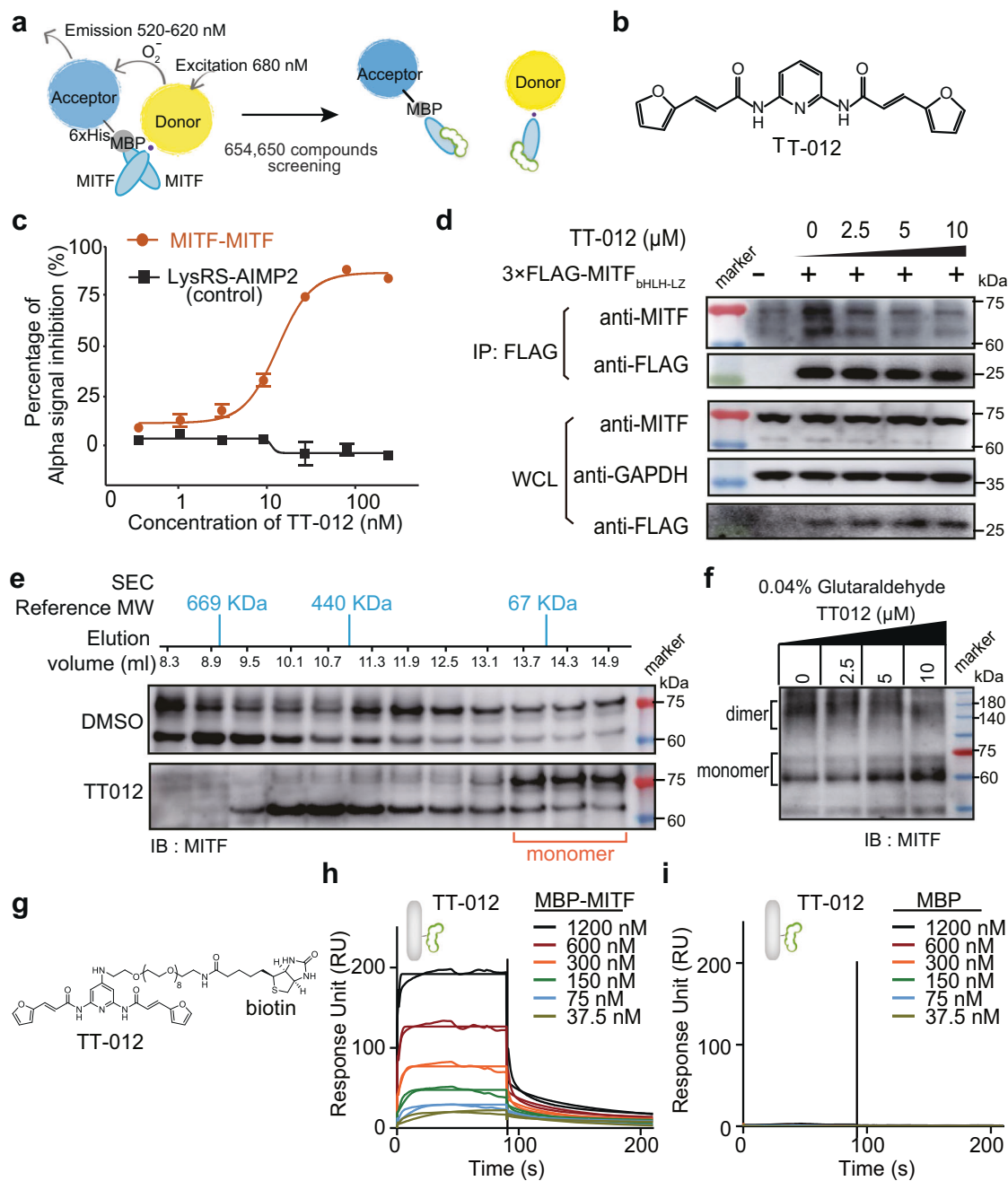
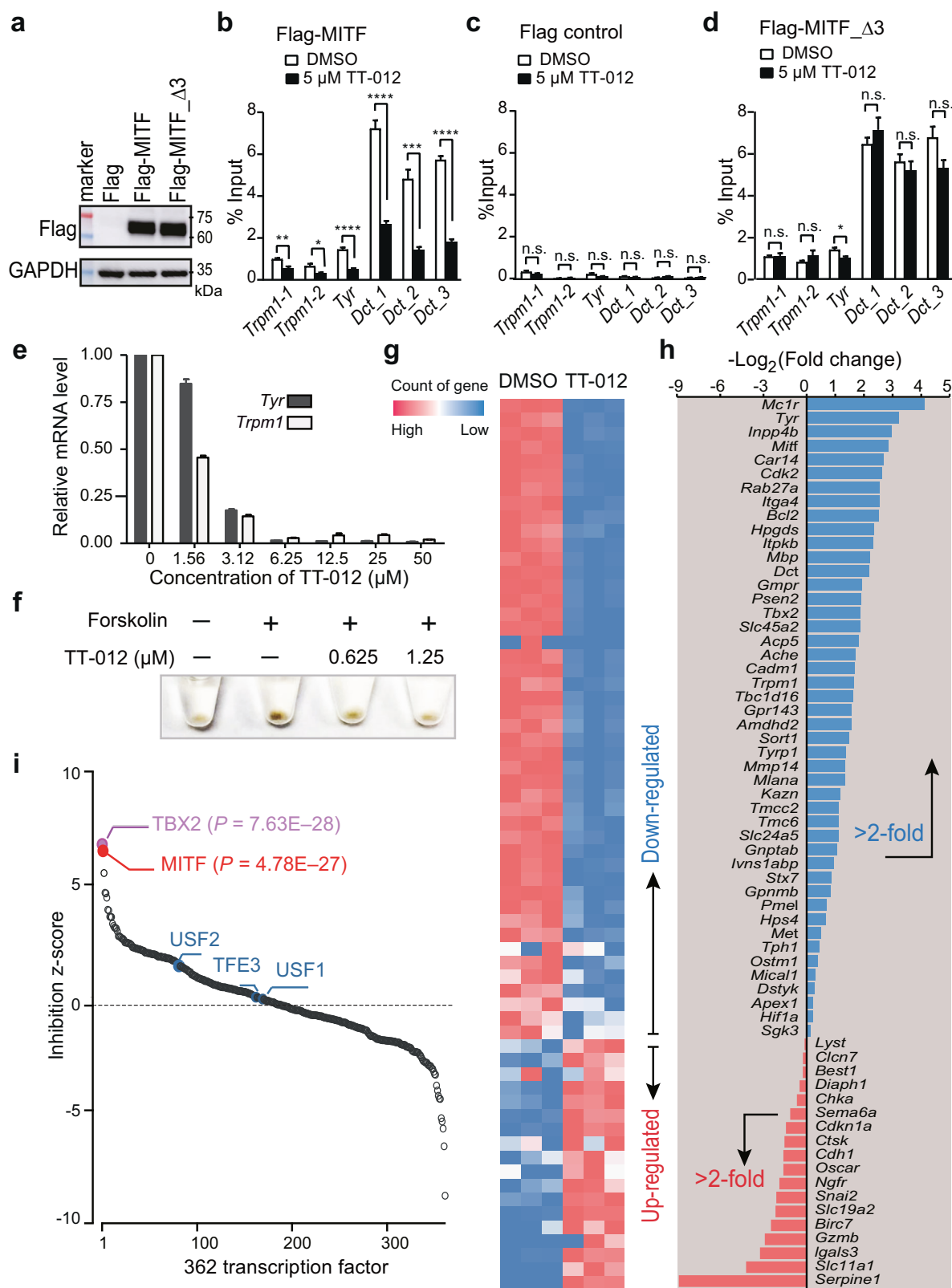


**Fig. 4** High-throughput screening identifies a MITF dimer disruptor TT-012. **a** Schematic diagram of the MITF Dimerization-based AlphaScreen (MIDAS) assay for screening MITF dimer disruptors. **b** Chemical structure of TT-012: (2E,2'E)-N,N'-(pyridine-2,6-diy)bis(3-(furan-2-yl)acrylamide). **c** Titration of TT-012 in the MIDAS assay and the control AlphaScreen assay that detects the interaction between biotin-tagged AIMP2 and his-tagged LysRS. TT-012 inhibited the AlphaScreen signal generated by MITF–MITF dimerization with an IC<sub>50</sub> of 13.1 nM, but showed no inhibition effect on the control assay. Error bars represent the SEMs of three repeats. **d** IP analysis of the effect of TT-012 on the interaction between 3× Flag-MITF<sub>bHLH-LZ</sub> and endogenous MITF using anti-Flag antibody. The lysates of B16F10 cells stably expressing 3× Flag-MITF<sub>bHLH-LZ</sub> were aliquoted and incubated with gradient TT-012 before IP. IP, immunoprecipitation; WCL, whole cell lysates. **e** SEC analysis of the effect of TT-012 on the state of endogenous MITF. B16F10 cells were treated with 10 μM TT-012 or DMSO for 1 h before cell lysis and fractionation. TT-012 increased the monomer form of endogenous MITF as immunoblotted by anti-MITF antibody. **f** Cross-linking analysis of the effect of TT-012 on the amount of cross-linked endogenous MITF dimer. B16F10 cells were treated with gradient TT-012 or DMSO for 1 h before cell lysis and glutaraldehyde treatment. TT-012 dose-dependently attenuated the cross-linked endogenous MITF dimer, while increased the monomer form of MITF. **g** Chemical structure of biotin-labeled TT-012. **h**, **i** SPR experiments measuring the binding ability of the MBP-fused bHLH-LZ domain of MITF (MBP-MITF) with TT-012 that immobilized on chip through biotin. MBP-MITF interacts with TT-012 with  $k_{on} = 3.24 \times 10^6 \pm 2.7 \times 10^5 \text{ M} \cdot \text{s}^{-1}$ ,  $k_{off} = 0.050 \pm 0.004 \text{ s}^{-1}$ , and  $K_d = 15.5 \text{ nM}$  (**h**). The interaction between TT-012 and MBP control cannot be detected (**i**).

consistently increased the monomer form of endogenous MITF, while decreasing the dimer form of endogenous MITF (Fig. 4*f*; Supplementary information, Fig. S11). Together, these results confirm that TT-012 prevents the formation of MITF dimer.

To evaluate the interaction between TT-012 and MITF, we performed surface plasmon resonance (SPR) experiments with the MITF<sub>WT</sub> immobilized on a chip which showed that TT-012 interacted with MITF<sub>WT</sub> with  $k_{on} = 1546 \pm 19 \text{ (M} \cdot \text{s})^{-1}$ ,  $k_{off} = 7.2 \times 10^{-4} \text{ s}^{-1}$ .



$4 \pm 1.6 \times 10^{-5} \text{ s}^{-1}$ , and a  $K_d$  of 463.2 nM (Supplementary information, Fig. S12a). Importantly, TT-012 showed reduced ability to bind the MITF $_{\Delta 3}$  mutant, which forms a more stable dimer (Supplementary information, Fig. S12b). In contrast, the MITF dimer-disrupting mutation N278D could still bind TT-012 (Supplementary

information, Fig. S12c). These results support the idea that the hyperdynamic nature of MITF is essential for TT-012 function. The immobilization process of MITF on the chip may limit its dynamic conformation and the interaction with TT-012, leading to the diminishing of the binding affinity between the two. To overcome

**Fig. 5 TT-012 suppresses MITF activity and function in melanoma cells.** **a** B16F10 cells transiently transfected with 3x Flag-MITF, 3x Flag-MITF<sub>Δ3</sub> and 3x Flag control were immunoblotted with anti-Flag antibody. **b–d** ChIP analysis of the occupancy of Flag-MITF (**b**), Flag control (**c**), and Flag-MITF<sub>Δ3</sub> (**d**) on the promoters of MITF target genes including *Tyr*, *Trpm1*, and *Dct* after TT-012 treatment. For gene containing multiple E/M boxes in the promoter region, quantitative PCR analysis was performed for each E/M box sequence which was numerically labeled as \_1, \_2 or \_3. Error bars represent the SEMs of three repeats. \* $P < 0.05$ ; \*\* $P < 0.01$ ; \*\*\* $P < 0.001$ ; \*\*\*\* $P < 0.0001$ ; ns, no significant; Student's unpaired *t*-test. **e** Quantitative RT-PCR assay detecting the mRNA levels of the MITF downstream genes *Tyr* and *Trpm1* in B16F10 melanoma cells treated with increasing doses of TT-012 for 8 h. Error bars represent SEMs of three repeats. **f** TT-012 inhibited the forskolin-induced pigmentation in a dose-dependent manner. **g** RNA-seq analysis of B16F10 cells treated with 5 μM TT-012 or DMSO control ( $n = 3$ ). A heatmap for transcripts from 64 reported MITF target genes is shown in the same order as in **h**. **h** Shown is –Log<sub>2</sub> (Fold change) (TT-012 treated/DMSO-treated) for transcripts from MITF target genes. **i** Using the “Upstream Regulator Analysis” function of IPA, MITF was identified as the second significantly inhibited transcription factor out of a total of 362 transcription factors after treating B16F10 cells with 5 μM TT-012 ( $P = 4.78E-27$ ). TBX2 (*TBX2* is a direct MITF target gene) was identified as the most significantly inhibited transcription factor ( $P = 7.63E-28$ ). The other MiT/TFE family members are less affected (TFE3 was ranked 136th, USF1 142nd, and USF2 79th). The transcription factor TFEB is not predicted to be affected according to IPA.

this limitation of the experiment, we further synthesized a biotin-labeled TT-012 (Fig. 4g), and immobilized TT-012 on a chip through the biotin tag. The results showed that the MBP fused MITF<sub>bHLH-LZ</sub> (MBP-MITF<sub>bHLH-LZ</sub>) interacted with TT-012 with a  $K_d$  of 15.5 nM (Fig. 4h), while MBP control had no binding signal (Fig. 4i). Removing MBP decreased the interaction between MITF<sub>bHLH-LZ</sub> and TT-012 by 3.7-fold ( $K_d$  of 57.7 nM), implying that MBP can stabilize the bHLH-LZ domain of MITF (Supplementary information, Fig. S13a). We further purified the basic region, HLH region and LZ region, and measured their interactions with TT-012, respectively. The results showed that only the complete bHLH-LZ domain could bind to TT-012 effectively while the basic and LZ regions did not bind to TT-012, and the HLH region maintained a weak binding ability to TT-012 (Supplementary information, Fig. S13b-d). These results indicate that MITF may bind to TT-012 through the HLH region, and that the complete bHLH-LZ domain is required to form effective binding.

### TT-012 inhibits MITF activity in melanoma cells

To assess if TT-012 could disrupt the interaction between MITF and M-box DNA in cells, we performed chromatin immunoprecipitation (ChIP) analysis in B16F10 cells that transiently express 3x Flag-tagged MITF, 3x Flag-tagged MITF<sub>Δ3</sub>, and Flag control (Fig. 5a). The results showed that TT-012 significantly disrupted the interaction between MITF and the promoter of MITF target genes, *Trpm1*, *Tyr*, and *Dct* (Fig. 5b, c). Of note, TT-012 had no significant effect on the interaction between Flag-MITF<sub>Δ3</sub> and the aforementioned DNAs, confirming that TT-012 can only inhibit the interaction between dynamic MITF and the promoter of its target genes (Fig. 5c, d).

We further performed real-time reverse transcription PCR (RT-PCR) assay to quantify the mRNA levels of MITF downstream genes in B16F10 melanoma cells after 8 h of incubation with TT-012. The result indicated that TT-012 decreased the mRNA level of MITF target genes (*Tyr* and *Trpm1*) with IC<sub>50</sub> values less than 3.12 μM, according to RT-PCR analysis on melanoma cells treated with TT-012 or DMSO (Fig. 5e). In addition, TT-012 suppressed the MITF-mediated melanin formation which is activated by forskolin (Fig. 5f). Together, these results indicate that TT-012 inhibits the transcriptional activity and cellular function of MITF.

To investigate the impact of TT-012 on the broader landscape of the MITF transcriptional network, we performed RNA sequencing (RNA-Seq) analysis of the B16F10 cells treated with DMSO vehicle or 5 μM TT-012 (Fig. 5g, h). 33 out of the 64 reported MITF downstream genes<sup>8,37–43</sup> were down-regulated by more than 2-fold. Among them, the key genes in melanosome biogenesis and function, such as *Mcl1R*, *Mlana*, *Tyr*, *Trpm1*, *Dct*, *Rab27a*, and *Slc45a2*, were down-regulated by 3–17-fold after TT-012 treatment. *Bcl2*, *Cdk2*, and *Tbx2* are essential genes involved in melanocyte/melanoma survival and proliferation, and were down-regulated after TT-012 treatment by 3–6-fold. *Diaph1* and *Cdkn1a*, whose expression products inhibit cell cycle, were up-regulated by

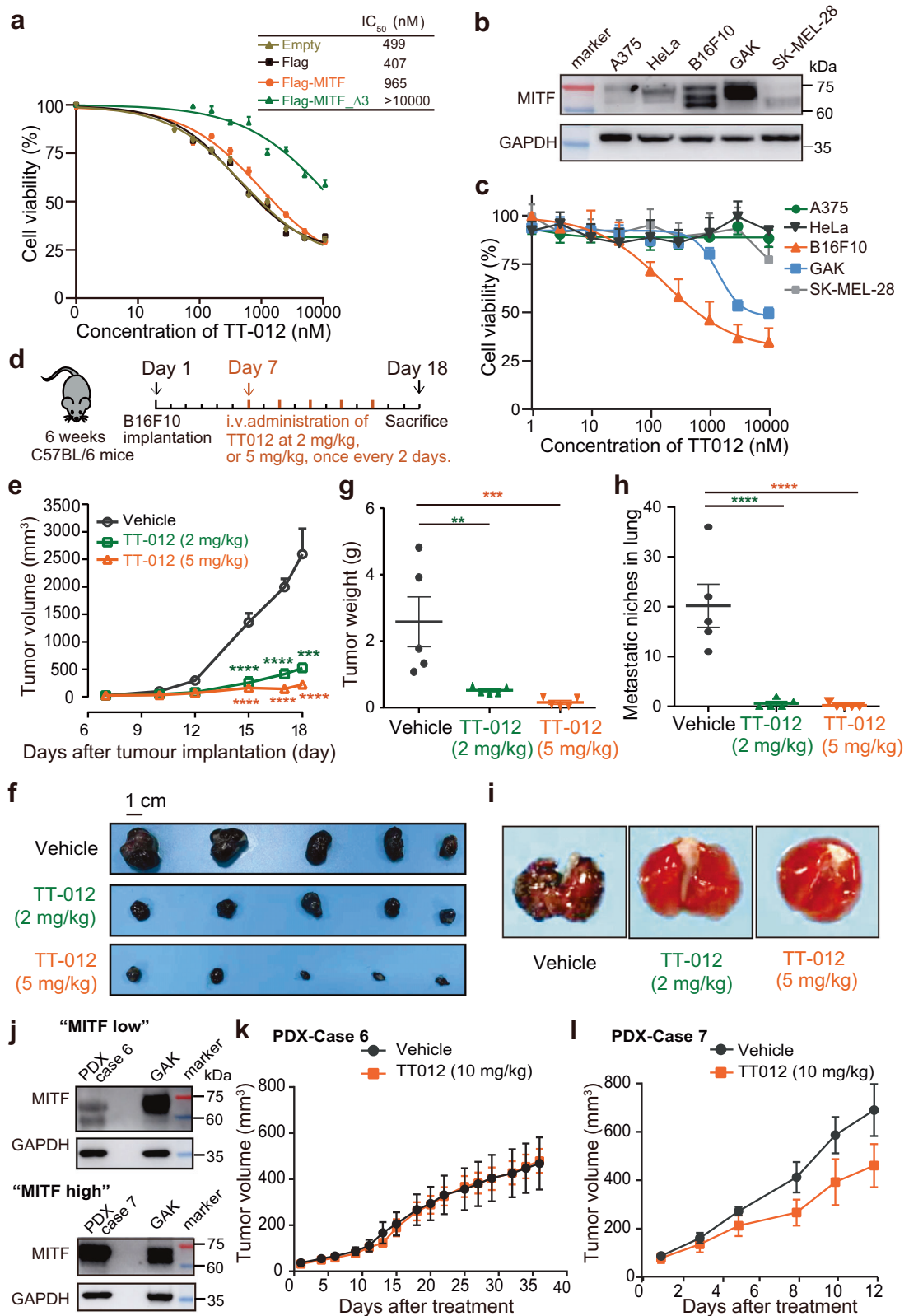
1.4-fold and 2.7-fold, respectively. Of note, *Mitf* mRNA itself was significantly down-regulated (7.2-fold), resonating a previous finding that MITF activates its own gene transcription,<sup>43</sup> and endowing an additional advantage for directly targeting MITF. Together, these results indicate that TT-012 systematically inhibits the transcription of MITF downstream genes.

Using the “Upstream Regulator Analysis” function of Ingenuity Pathway Analysis (IPA), MITF was identified as the second significantly inhibited transcription factor out of a total of 362 transcription factors ( $P = 4.78E-27$ ) after TT-012 treatment (Fig. 5i). *TBX2*, a direct MITF target gene, which encodes a key developmental regulator of cell identity and an antisenescence factor in melanoma, was identified as the most significantly inhibited transcription factor with downstream genes that have the most significantly inhibited expression ( $P = 7.63E-28$ ) (Fig. 5i). The other MiT/TFE family members TFE3, USF1, and USF2 were much less affected, while TFEB was not predicted to be affected (Fig. 5i). Therefore, TT-012 treatment selectively inhibited the MITF-mediated transcriptional network at a genomic scale.

### TT-012 inhibits MITF-high melanoma cell growth in vitro and in vivo

Inhibition of MITF activity in melanoma cell lines was reported to be able to inhibit cell proliferation.<sup>9</sup> We also observed that siRNA-mediated knockdown of *MITF* reduced the viability of melanoma B16F10 cells (Supplementary information, Fig. S14). Consistently, TT-012 inhibited B16F10 melanoma cell growth with an IC<sub>50</sub> of 499 nM (Fig. 6a). Overexpression of Flag-MITF reduced the antigrowth effects of TT-012 by over two fold and overexpression of Flag-MITF<sub>Δ3</sub> further decreased the antigrowth effects of TT-012 by over 24-fold (Fig. 6a). In addition, we assessed the effectiveness of TT-012 against cancer cells with different levels of MITF expression (Fig. 6b), and observed that TT-012 specifically inhibited melanoma cells with high MITF expression such as B16F10 and GAK, but not cells with low MITF expression, such as A375, HeLa, and SK-MEL-28 (Fig. 6c). Together, these results demonstrate that TT-012 exerts cytotoxic activity largely through the inhibition of MITF.

Next, we evaluated the anti-melanoma activity of TT-012 in vivo. When B16F10 tumors in mice reached a palpable size (50 mm<sup>3</sup>, day 7), the mice were administered TT-012 (2 mg/kg or 5 mg/kg, loaded into micelle nanoparticles to improve the solubility) or vehicle control through intravenous tail injection (Fig. 6d). After administration of 5 shots, both concentrations of TT-012 potently suppressed tumor growth, with  $P < 0.0001$  (Fig. 6e, f). By the end of the experiment, the average tumor weight of the TT-012-treated group was reduced by 79.7% (2 mg/kg) and 93.9% (5 mg/kg) compared to that of the vehicle-treated group (Fig. 6g). In the pulmonary metastasis model (Supplementary information, Fig. S15), after 18 days of TT-012 treatment, the mice administered with 2 mg/kg TT-012 displayed a significant decrease in metastatic burden in the lung ( $P < 0.0001$ ) compared to those administered with the vehicle control (Fig. 6h, i).



Increasing TT-012 to 5 mg/kg further enhanced the effect, and the metastatic burden decreased by ~99% compared with that of the vehicle control ( $P < 0.0001$ ) (Fig. 6h, i). We further established two patient-derived xenograft (PDX) models with low MITF expression (PDX-case 6) and high MITF expression (PDX-case 7), respectively (Fig. 6j). TT-012 attenuated xenograft tumor growth of PDX-case 7

with high MITF, but had no effect on PDX-case 6 with low MITF (Fig. 6k, l). Independent xenograft experiments further confirmed that both intratumoral and intravenous injection of TT-012 decreased the xenograft tumor growth of PDX-case 7 (Supplementary information, Fig. S16). These data show that TT-012 has anticancer activity against tumors with high expression of MITF.

**Fig. 6 TT-012 inhibits MITF-high melanoma growth in vitro and in vivo.** **a** TT-012 inhibited B16F10 melanoma cell growth in the MTT assay. B16F10 cells or B16F10 cells stably expressing Flag, Flag-MITF\_WT, or Flag-MITF $\Delta$ 3 were treated with increasing doses of TT-012 for 72 h. Error bars represent the SDs of six repeats. **b** Western blot detecting the MITF expression levels in different cancer cell lines. **c** MTT assay showing that TT-012 selectively inhibited the growth of melanoma cells B16F10 and GAK with high expression of MITF, but had no significant activity against cells A375, HeLa and SK-Mel-28 with low expression of MITF. **d, e** B16F10 melanoma-bearing C57BL/6 mice were intravenously injected with TT-012 (2 mg/kg or 5 mg/kg) or vehicle control. The tumor volumes were measured. Error bars represent the SDs from  $n = 5$  replicates. \*\*\* $P < 0.001$ , \*\*\*\* $P < 0.0001$  by one-way ANOVA with Dunnett's correction for multiple pairwise comparisons. **f, g** The weights and photographs of the excised tumors from the experiment described in **d, e**. \*\* $P < 0.01$ , \*\*\* $P < 0.001$  by one-way ANOVA with Dunnett's correction for multiple pairwise comparisons. **h** The number of lung metastatic niches decreased in mice treated with 2 mg/kg or 5 mg/kg of TT-012 compared to vehicle-treated mice. Error bars represent the SDs from  $n = 5$  replicates. \*\*\*\* $P < 0.0001$  by one-way ANOVA with Dunnett's correction for multiple pairwise comparisons. **i** Representative photographs of lungs from TT-012 (2 mg/kg, 5 mg/kg)-treated and vehicle-treated mice in melanoma pulmonary metastasis model as described in supplementary information Fig. S15. **j** Western blots detecting the MITF expression levels in PDX biopsies from case 6 and case 7. The GAK melanoma cells were used as control. **k, l** Tumor volume quantification for PDX-case 6 (**i**) and PDX-case 7 (**j**) which were intravenously injected with vehicle control or TT-012 (10 mg/kg) three times weekly. Error bars represent the SEMs from  $n = 5$  or 6 replicates.

The body weight of the TT-012-treated C57BL/6 mice was not significantly different as compared with the body weight of vehicle-treated mice (Fig. 7a). To further test the possible effect of TT-012 on immune cells, we isolated and analyzed major immune cells from peripheral blood, lymph nodes, bone marrow, thymus, and spleen. The results showed that the major lymphoid and myeloid subsets were well tolerant to TT-012 treatment (Fig. 7b–e). We also examined the effect of TT-012 on liver function by testing the glutamate pyruvate transaminase (GPT) and alkaline phosphatase (ALP) levels in the blood, and no significant changes were observed, indicating that TT-012 did not cause apparent liver damage (Fig. 7f).

Together, these results show that TT-012 effectively inhibits melanoma growth and metastasis, and has tolerable toxicity to liver and immune cells, indicating that it is a good lead molecule for the development of anti-melanoma drugs.

## DISCUSSION

Transcription factors are a major class of cancer dependencies that have been estimated to account for 20% of oncogenes in cancer.<sup>44,45</sup> Approximately 10% of the drugs approved by the United States Food and Drug Administration directly target the nuclear receptor transcription factors.<sup>46</sup> However, transcription factors outside the nuclear receptor class, such as the bHLH-LZ family, are generally thought to be undruggable.<sup>47</sup> In this study, we explored an effective approach to suppress the bHLH-LZ transcription factor MITF, the lineage-survival/addiction oncogene of melanoma.

The disruptive effects of the internal LZ mutations and small molecular dimer inhibitors may be attributed to the energy barrier between the dimer and monomer forms of MITF. Single helix monomer structures are extremely unstable by themselves,<sup>48</sup> for instance, a bHLH-LZ protein such as MYC is known to exist as nonstructured random coils in monomer form with lower energy on the folding tunnel.<sup>49</sup> In contrast, all current results indicate that MITF pre-exists as a dimer. The measured dimerization affinity of MITF (30 nM) is stronger or close to its affinity for binding to DNA (113 nM), suggesting that the free MITF in cells may be present largely in the dimer form. The seemingly contradictory property of MITF as a tighter but also structurally fragile dimer suggests a strong evolutionary benefit/requirement for this strict subfamily specificity that would inevitably sacrifice structural stability. With mutations or compounds weakening the dimer, the equilibrium is shifted toward the nonstructured monomer form, thus trapping MITF in a lower energy state. The resulting energy barrier effectively prevents MITF from refolding and hence completely abolishes DNA-binding and transcription activities (Fig. 7g). Therefore, through an allosteric mechanism on the protein folding landscape, disease-related mutations or dimer-disrupting compounds that shift the MITF structure to a monomer would enhance their inhibitory effects on MITF function.

Low MITF melanomas have been hypothesized to be less proliferative and more invasive (metastatic). The observation that

TT-012 can decrease both tumor volume and lung metastasis is likely related to the ‘invasive/high MITF’ nature of transplanted B16F10 cells. This also indicates that the output of MITF inhibition by a chemical compound is different from the outcome in melanoma cells that originally had low expression levels of MITF.

While MITF is known as one of the most crucial oncogenes in melanoma, its role in invasion is not fully understood. On the one hand, MITF may inhibit metastasis, because MITF is expressed at low levels in some invasive human melanoma cells.<sup>50</sup> On the other hand, some high MITF-expressing cell lines display invasive behavior in 3D extracellular matrix systems.<sup>51</sup> MITF regulates key intermediates required for metastasis, including c-MET which mediates hepatocyte growth factor-stimulated melanoma cell invasion,<sup>18</sup> BCL2 which promotes invasion and lung metastasis by inducing matrix metalloproteinase-2.<sup>2,52</sup> The expressions of these genes were inhibited by TT-012 (Fig. 5h) and may contribute to the anti-metastasis activity of TT-012 in the B16F10 animal model.

MITF is involved in multiple pathophysiological processes, such as allergy response and autophagy.<sup>53–56</sup> In addition, MITF was decoupled from regulation in pancreatic ductal adenocarcinoma to support the high level of autophagy, and shMITF significantly suppressed the growth of multiple pancreatic cancer cell lines.<sup>57</sup> Dysregulated MITF has also been reported in clear cell sarcoma.<sup>58</sup> Thus, inhibition of MITF by small-molecule TT-012 may also present a novel approach to benefit treatment for a range of diseases.

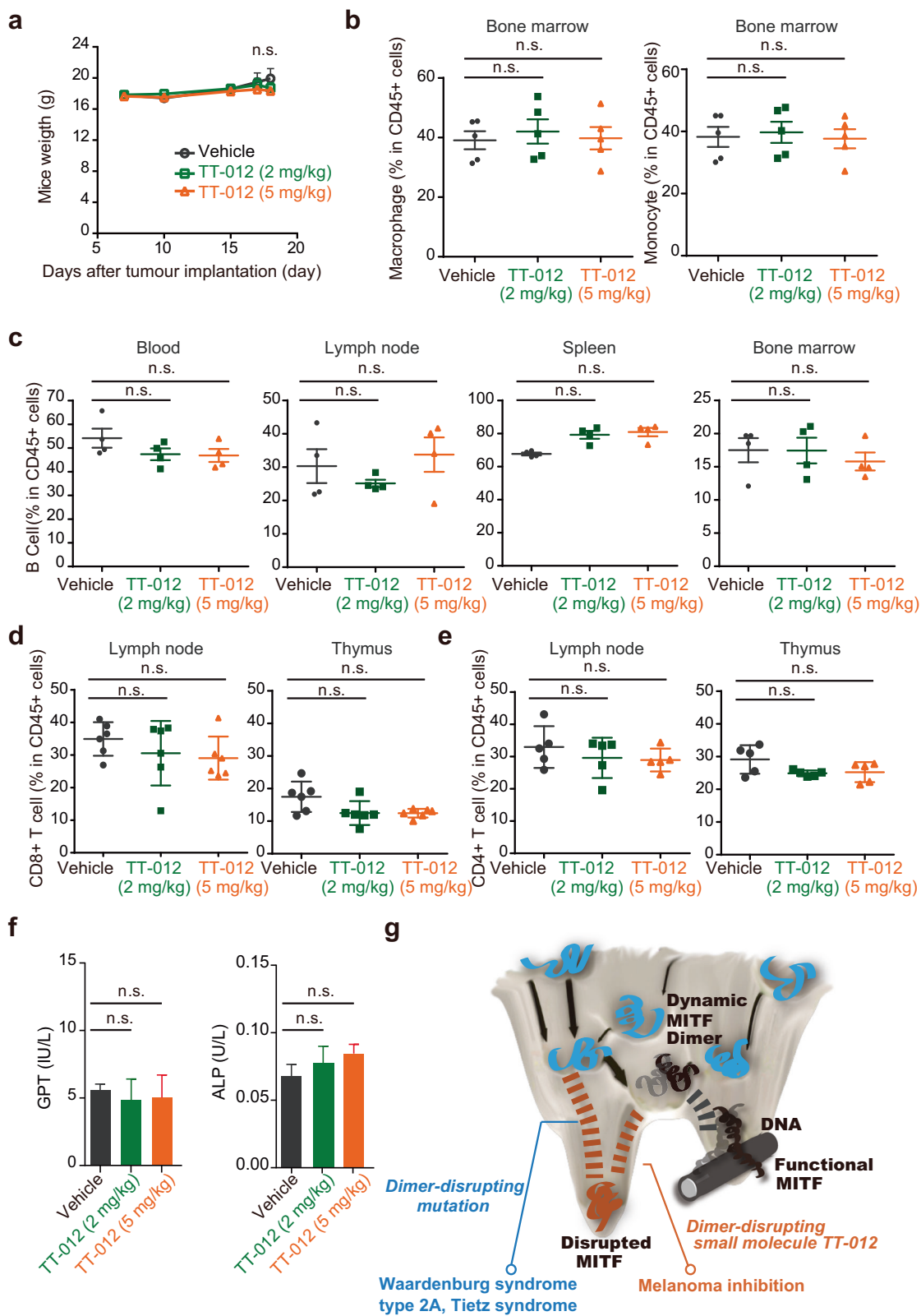
## MATERIAL AND METHODS

### Protein preparation

For crystallization, the HLH-LZ (residues 217–288) and bHLH-LZ (residues 199–288) of human MITF isoform M1 were constructed with an N-terminal 6x His-tag and a C-terminal Trbp111 protein in a pHisTEV vector. For Crystals II and III, an N278C mutation was introduced to the bHLH-LZ construct to improve the crystal diffraction. For MITF $\Delta$ 3 crystal, the HLH-LZ region of human MITF isoform M1 (residues 217–288) with  $^{264}$ AKE $^{266}$  removed was constructed with an N-terminal 6x His-MBP in a pHis-MBP-TEV vector. All the plasmids were induced to be expressed in the bacterial strain BL21 (DE3) with 0.2 mM isopropylthio-galactoside (IPTG) at 16 °C for 20 h, and purified to homogeneity with a Ni-HiTrap affinity column. The 6x His-tag or 6x His-MBP tag was removed by TEV protease, and the cleaved protein was passed through a Ni-HiTrap column or a HiTrap MBP column followed by purifications with a HiTrap SP Sepharose column and a size exclusion S75 column (GE Healthcare).

For MBP-fused MITF proteins, the bHLH-LZ domain (residues 199–288) of human MITF isoform M1 was first constructed in a pHis-MBP-TEV vector to generate the MBP-MITF\_WT protein. MBP-fused MITF $\Delta$ 3, MITF mutants including N210K, H209R, Del217, R217I, D222N, I224S, S250P, Y253C, R259Stop, N278D, L281A, L281R, L281K were all generated based on this construct. For MBP-fused MAX proteins, the bHLH-LZ domain of human MAX (residues 17–113, isoform 1) was constructed in a pHis-MBP-TEV vector to generate the MBP-MAX\_WT and site-directed mutagenesis on this construct was performed to generate MBP-MAX\_L95A.

To purify MITF\_WT, MITF\_basic, MITF\_HLH, MITF\_LZ, and MITF $\Delta$ 3 proteins, the related MBP-fused proteins were first expressed and purified



to homogeneity with a Ni-HiTrap affinity column. The 6x His-MBP tag was then removed by TEV protease, and the cleaved protein was passed through a HiTrap MBP column followed by purifications with a HiTrap SP Sepharose column and a size exclusion S75 column (GE Healthcare).

To purify His-tagged bHLH-LZ domain (residues 199–288) of human MITF isoform M1, 6x His-MITF\_WT, 6x His-MITF\_N278D and 6x His-

MITF $\Delta$ 3 proteins were first expressed and purified to homogeneity with a Ni-HiTrap affinity column and a size exclusion S75 column (GE Healthcare).

For preparation of the 5-iodoacetamido-Fluorescein (5-IAF)-labeled proteins  $_{5\text{IAF}}\text{MITF\_WT}$ ,  $_{5\text{IAF}}\text{MITF\_}\Delta\text{3}$  and  $_{5\text{IAF}}\text{MAX\_WT}$ , a cysteine residue together with a GG linker was added to the C-termini of MBP-MITF\_WT, MBP-MITF $\Delta$ 3 and MBP-MAX\_WT. The MBP tag was removed by TEV

**Fig. 7 TT-012 has tolerable toxicity to liver and immune cells in mouse model.** **a** Analysis of body weight during treatment of the B16F10 melanoma-bearing mice with TT-012 (2 mg/kg, or 5 mg/kg) or vehicle control, from the experiment described in Fig. 6d. Error bars represent the SDs from  $n=5$  replicates. Student's unpaired two-tailed *t*-test was carried out, and no significant (n.s.) change was observed. **b–e** Cell frequencies of major lymphoid and myeloid subsets in the bone marrow, spleen, peripheral blood, lymph nodes and thymus of C57BL/6 mice at the end of treatment with TT-012 (2 mg/kg or 5 mg/kg) or vehicle control, using the procedure described in Fig. 6d. Monocytes and macrophages were analyzed in bone marrow (**b**); CD19<sup>+</sup>B220<sup>+</sup> B cells were analyzed in peripheral blood, lymph nodes, spleen and bone marrow (**c**); CD3<sup>+</sup>CD8<sup>+</sup> T cells were analyzed in lymph nodes and thymus (**d**); CD3<sup>+</sup>CD4<sup>+</sup> T cells were analyzed in lymph nodes and thymus (**e**). Error bars represent the SDs from  $n=5$  replicates. Student's unpaired two-tailed *t*-test was carried out and no significant change was observed. **f** C57BL/6 mice were treated with TT-012 (2 mg/kg or 5 mg/kg) or vehicle control by using the procedure described in Fig. 6d. GPT and ALP in peripheral blood were examined to show the liver injury response. Error bars represent the SDs from  $n=3$  replicates. Student's unpaired two-tailed *t*-test was carried out and no significant change was observed. **g** The distinct dynamic feature of MITF makes carriers of dimer-disrupting mutations prone to human diseases WS2 and TS, while it also provides a specific strategy to therapeutically inhibit MITF. The arrows represent the folding process of MITF, and each pit describes the different energy states that MITF may experience during folding. MITF dimers in the correctly folded state can bind DNA, and MITF in the misfolded state induced by dimer-disrupting mutations or dimer-disrupting small molecule TT-012 cannot bind DNA and function biologically.

protease and the proteins were purified as described above. Then, the sulphydryl cysteine end of the protein was labeled with Thermo Scientific™ 5-IAF per the manufacturer's instructions.

### Crystallization, data collection, and structure refinement

Crystallization was performed by the sitting drop method. For Crystal I, the crystallization drop was prepared by mixing 0.15  $\mu$ L of the protein solution (20 mg/mL) with 0.15  $\mu$ L of precipitant solution containing 50 mM HEPES, pH 7.5, 0.2 M KCl, and 27%–30% PO/OH. For Crystal II, the drop was prepared by mixing 0.15  $\mu$ L of the protein solution (20 mg/mL) with 0.15  $\mu$ L of precipitant solution containing 0.1 M sodium acetate, pH 4.5, and 2.0 M ammonium sulfate. For Crystal III, the protein was mixed with 16 bp double-stranded E-box DNA from *Mus musculus* MCP6 containing a single nucleotide overhang at each 3' end (5'-GGGACACATGTTACAG-3', 5'-TGTAAACATGTGCCCC-3'). The MITF-DNA complex was purified by a size exclusion S75 column (GE Healthcare). The crystallization drop was prepared by mixing 0.15  $\mu$ L of the complex solution (25 mg/mL) with 0.15  $\mu$ L of precipitant solution containing 30% PEG4000, 0.1 M Tris-Cl, pH 8.5, and 0.2 M sodium citrate. For the MITF $\Delta$ 3 crystal, the crystallization drop was prepared by mixing 0.3  $\mu$ L of the protein solution (10 mg/mL) with 0.3  $\mu$ L of precipitant solution containing 1.8 M ammonium citrate, pH 7.0.

Crystals were collected after incubation at 18 °C for 7 days and were flash-frozen in liquid nitrogen for data collection with 70% reservoir solution and 30% glycerol. Diffraction datasets for Crystals I, II, and III were collected at LS-CAT beam lines at the Advanced Photon Source (APS, Argonne, IL). MITF $\Delta$ 3 crystal diffraction datasets were obtained at National Facility for Protein Science in Shanghai (NFPS) at Shanghai Synchrotron Radiation Facility (SSRF).<sup>59</sup>

The structure of Crystal I was first solved by single wavelength anomalous diffraction of soaked K<sub>2</sub>PtBr<sub>6</sub> at 3.3 Å resolution using the Phenix program, and then another nonsoaked crystal from the same construct was solved by molecular replacement and refined to a resolution of 3.0 Å. The structures of Crystals II and III and MITF $\Delta$ 3 were solved by molecular replacement using Crystal I with the Molrep program.<sup>60</sup> Iterative model building and refinement were performed using Coot and Phenix.<sup>61,62</sup> Data collection and refinement statistics of all three structures are given in Supplementary information, Table S1. Atomic coordinates and structure factors for the reported crystal structures have been deposited in the Protein Data Bank under accession numbers 7D8R (Crystal I), 7D8S (Crystal II), 7D8T (Crystal III), and 7EOD (MITF $\Delta$ 3).

### MBP pull-down assay

Equal amounts of individual MBP-MITF (the bHLH-LZ domain of human MITF isoform M1, residues 199–288, WT or mutants) or MBP control were incubated with nontagged MITF\_WT, and 10  $\mu$ L of amylose beads (New England Biolab, Ipswich, MA) in pull-down buffer (20 mM HEPES, pH 7.5, 200 mM NaCl) for 1 h at 4 °C. After washing with 40  $\mu$ L pull-down buffer for 3 times, the bead-bound components were analyzed by coomassie brilliant blue staining.

### Real-time kinetic binding assay

The interaction between M-box DNA (biotin-CAGTCATGTGCT (sense); AGCACATGACTG (anti-sense)) and MBP-MITF (the bHLH-LZ domain of human MITF, WT or mutants) was tested by the ForteBio Octet Red system (ForteBio, Inc., Menlo Park, CA). The 5'-biotinylated M-box DNA duplexes were immobilized onto streptavidin biosensors (ForteBio, Inc.), and the association and dissociation of the DNA on MBP-MITF\_WT or indicated

MBP-MITF\_mut was monitored in parallel for 180–420 s in binding buffer containing 1× PBS, 0.01% BSA, 0.002% Tween, 1 mM MgCl<sub>2</sub>.

### Thermal stability assay

A Chirascan Circular Dichroism Spectrometer (Applied PhotoPhysics) was used to obtain melting curves of the MITF\_WT (bHLH-LZ domain of human MITF isoform M1, residues 199–288) and MITF $\Delta$ 3 (removing 264AKE<sub>266</sub> of MITF as mentioned above), with or without E-box DNA from *Mus musculus* MCP6 promoter (5'-GGGACACATGTTACAG-3', 5'-TGTAAACATGTGCCCC-3'). All experiments were carried out with 10  $\mu$ M protein in 10 mM phosphate-Na buffer, pH 7.2, 50 mM NaF, with or without 10  $\mu$ M E-box DNA. The CD signal at 222 nm was monitored as the temperature increased in 1 °C increments from 20 °C to 85 °C.

### Fluorescence anisotropy assay

Fluorescence polarization measurements were carried out using a SpectraMax M5 microplate reader (Molecular Devices, Sunnyvale, CA). To determine the dimer formation of MITF, the  $\text{S}_{14}F$ MITF\_WT (bHLHLZ domain of human MITF, final concentration of 20 nM) was mixed with a gradient of MBP-MITF\_WT or MBP-MITF mutant as indicated (0.625–1280 nM) in buffer containing 20 mM HEPES, pH 7.5, 200 mM NaCl, and 5% glycerol. To determine the dimer formation of the transcription factor Max, the  $\text{S}_{14}F$ MAX\_WT (bHLHLZ domain of human MAX, final concentration of 20 nM) was mixed with a gradient of MBP-MAX\_WT or MBP-MAX\_L95A (0.625–1280 nM). The mixtures were incubated at 4 °C overnight before measurement. An excitation beam at 494 nm and emission at 518 nm were used to detect the fluorescence anisotropy.

To determine the DNA binding activity of the MITF<sub>bHLHLZ</sub>Trbp111 and MITF<sub>bHLHLZ</sub> (also the MITF\_WT), the FAM-labeled M-box DNA (5'-FAM-TCAGTCATGTGCTT-3', and the complementary DNA sequence was 5'-AAAGCACATGACTGA-3', final concentration 5 nM) was mixed with a gradient of MITF<sub>bHLHLZ</sub> or MITF<sub>bHLHLZ</sub>Trbp111 (final concentration 0–800 nM) in buffer containing 20 mM HEPES, pH 7.5, 200 mM NaCl, 1 mM MgCl<sub>2</sub> and 2.5% glycerol. The mixtures were incubated at 4 °C overnight before measurement. An excitation beam at 480 nm and emission at 535 nm were used to detect the fluorescence anisotropy.

The binding affinity  $K_d$  was calculated using the equation with receptor depletion:

$$A = A_f + (A_b - A_f) \times \frac{(L_T + K_d + R_T) - \sqrt{(L_T - K_d - R_T)^2 - 4L_T R_T}}{2L_T}$$

$L_T$  = the total added concentration of ligand;  $A$  = the experimental anisotropy;  $A_f$  = the anisotropy for the free ligand;  $A_b$  = the anisotropy for the fully bound ligand.<sup>63</sup>

### Alpha assay

The MITF dimerization-based AlphaScreen assay was performed following the previous study.<sup>36</sup> In general, the assay was set up in a 20  $\mu$ L reaction volume in Optiplate-384HS plates (PerkinElmer) under green light conditions at room temperature in triplicate. The reaction buffer contained 50 mM HEPES, pH 7.4, 250 mM NaCl, 0.1% Tween, and 0.1% BSA. MBP-MITF protein (residues 199–288, final concentration 20 nM) and AlphaScreen receptor beads (conjugated with anti-His antibody, final concentration 10  $\mu$ g/mL) were dispensed into the plate through a BioRAPTR FRD automated dispenser (Beckman Coulter). Gradient TT-012 was pinned into

the plates and incubated at 4 °C overnight. Then, biotin-MITF (199–288) (final concentration 5 nM) and AlphaScreen donor beads (conjugated with streptavidin, final concentration 10 µg/mL) were further dispensed into the plate and incubated for 2 h before reading on a PerkinElmer EnVision 2104 at wavelengths 520–620 nm. The alpha signal between LysRS and AIMP2 was performed as control.

### SEC assay

B16F10 cells were incubated with 10 µM TT-012 or DMSO control for 1 h. After washing cells with ice-cold PBS, the cells were harvested and lysed in radioimmunoprecipitation assay (RIPA) buffer containing 50 mM Tris, pH 7.4, 150 mM NaCl, 1% NP-40, phosphatase inhibitor (Bimake, B15001-A, B15001-B), and 1× protease inhibitor cocktail (Bimake, B14001). The cell lysate was digested with DNase I (Sangon Biotech) for 1 h at room temperature. The supernatant of each cell lysate was loaded onto a Superdex 200 Increase gel-filtration column (GE Healthcare, 10/300 GL) in buffer containing 20 mM HEPES, pH 7.5, 150 mM NaCl, with or without 10 µM TT-012. The fractions were mixed with 5× SDS sample buffer and boiled for SDS-PAGE and western blot analysis.

### Chemical cross-linking assay

B16F10 cells with 80% confluence were treated with TT-012 (concentration as indicated) or DMSO control for 1 h. Cells were harvested and lysed in ice-cold PBS buffer containing 1% NP-40, proteinase and phosphatase inhibitor cocktail (Bimake, B15001-A, B, B14001), and TT-012 (concentration as indicated) or DMSO control for 30 min. Total protein concentration was adjusted to 4 mg/mL. Glutaraldehyde (concentration as indicated, J&K Scientific, 902042) was added to the cell lysate and incubated for 30 min on ice, followed by the addition of 10% volume of 1 M Tris-HCl, pH 8.0 solution for quenching. Then the lysates were mixed with 5× SDS sample buffer and boiled for SDS-PAGE and western blot analysis.

### SPR assay

The binding affinity of TT012 to MITF was measured using Biocore T200 and Biocore 8 K (GE Healthcare). MITF\_WT (bHLH-LZ domain of human MITF isoform M1, residues 199–288), MITF\_N278D (bHLH-LZ domain with N278D mutation), and MITF\_Δ3 (bHLH-LZ domain removing 264AKE266) were immobilized at levels of 3600, 4400, and 4300 resonance units, respectively, with 10 mM sodium acetate buffer, pH 5.5 on a CM5 chip (GE Healthcare). TT-012 (0–20.0 µM) in PBS binding buffer, pH 7.4 containing 0.1% DMSO was flowed at a rate of 30 µL/min.

Biotin-tagged TT-012 was immobilized on SA chip (GE Healthcare) at levels of 280 resonance units. MBP-MITF\_WT, MBP control, MITF\_WT, MITF\_basic, MITF\_HLH, MITF\_LZ in PBS-P+ buffer (GE Healthcare) were flowed at a rate of 30 µL/min, respectively. Sensorsgrams were fitted to a simple 1:1 Langmuir interaction model (A + B ⇌ AB) using the Biocore T200 Evaluation Software analysis program.

### The cell lines

The mouse melanoma cell line B16F10 from the American Type Culture Collection was cultured in Dulbecco's modified Eagle's medium (DMEM, Invitrogen, Carlsbad, CA) supplemented with 10% of fetal bovine serum (FBS, ExCell Bio, Shanghai, China).

B16F10 cells stably expressing 3× Flag-MITF<sub>bHLHLZ</sub> from human melanocyte MITF melanocyte isoform M1 (residues 199–288), 3× Flag-MITF from mouse MITF melanocyte isoform M (residues 1–419), 3× Flag-MITF\_Δ3 from mouse MITF melanocyte isoform M (residues 1–419, removing 264AKE<sub>266</sub>) and 3× Flag control were generated with lentivirus using pMSCV-3× Flag-MITF<sub>bHLHLZ</sub>, pMSCV-3× Flag-MITF, pMSCV-3× Flag-MITF\_Δ3 and pMSCV empty vector, respectively. For packaging of the lentivirus, HEK293T cells were seeded in a 6-well plate in the Dulbecco's modified Eagle's medium (GE Healthcare, SH30243.01) supplemented with 10% fetal bovine serum (DMEM + 10% FBS). After the cells reached ~50% confluence, the culture medium was replaced with 1 mL of fresh DMEM + 10% FBS, and then, 250 µL Lipo3000 (Invitrogen, L3000-015)-DNA (2 µg pMSCV + 1 µg Gag-Pol-Rev + 1 µg VSV-G) mixture was added. The Lipo3000-DNA-containing medium was replaced with 2 mL fresh medium 12–16 h after transfection, and the lentivirus-containing medium was collected after 48 h. For lentiviral transduction, B16F10 cells were seeded in a 12-well plate to reach ~25% confluence in DMEM + 10% FBS. Then, the medium was replaced with the lentivirus-containing medium, and polybrene (Sigma, TR-1003) was added to each well at a concentration of 8 µg/mL. After 24 h, the transduction medium was replaced with fresh

medium. Stable cell lines were selected with 1.5–2 µg/mL puromycin (InvivoGen, QLL-38-04B), and the protein overexpression level was tested by western blot analysis.

### Co-IP assay

B16F10 cells stably expressing 3× FLAG-MITF<sub>bHLHLZ</sub> (from human melanocyte MITF melanocyte isoform M1, residues 199–288) were seeded in 6-cm cell culture dishes to reach ~95% confluence in DMEM and 10% FBS. Cells were washed by ice-cold PBS and lysed in RIPA buffer containing 50 mM Tris, pH 7.4, 150 mM NaCl, 1% NP-40, and 1× protease inhibitor cocktail (Bimake, B14001) for 30 min at 4 °C. Cell lysate was centrifuged at 12,000 rpm at 4 °C for 30 min. The supernatant was incubated with the indicated concentrations of TT-012 or DMSO control for 1 h, or indicated time on a vertical roller. Then, 20 µL of anti-FLAG magnetic beads (Bimake, B26102) were added into the system and incubated for 1 h at 4 °C. The beads were washed three times with PBST (Sangon Biotech, C520004-0001) and subjected to SDS-PAGE, followed by western blot analysis.

### Luciferase reporter assay

PCR products containing full-length human MITF (isoform M1, WT and mutants) were cloned into pcDNA3.1+ (Life Sciences, Grand Island, NY) using oligomer-introduced overhangs and homologous recombination and then were confirmed by sequencing. The MITF responsive promoter of the human *TRPM1* gene was cloned into pGL3 (Promega, Madison, WI) to drive the expression of luciferase, and the reactions were balanced with the appropriate amount of empty pcDNA3.1+ vector for a total DNA concentration of 200 ng/well. HEK293T cells were plated in 384-well format using CulturPlate (Perkin Elmer, Waltham, MA) and transfected 24 h prior to analysis using Lipofectamine (Life Technologies, Grand Island, NY) per the manufacturer's instructions. The cells were then lysed and exposed to luciferin using 30 µL/well BrightLight reagent (Perkin Elmer) and placed covered on a shaker for 10 min to ensure proper lysis. Titration of MITF mutants were compared to WT in the range of 0–128 ng/100 µL or 0–42.7 µg/30 µL in each well. Mutants were assayed in quintuplicate in an EnVision microplate luminometer (Perkin Elmer), and the results were analyzed statistically using Microsoft Excel.

### Depigmentation assay

B16F10 cells were plated in DMEM supplemented with 10% FBS at a density of  $1 \times 10^5$  cells per well in a 6-well plate. After 24 h of starvation in serum-free medium, cells were incubated with serum-free medium containing 0.2% DMSO (vehicle), 10 µM forskolin, or 10 µM forskolin (Millipore-Sigma) plus TT-012. After 3 days, the cells were detached with 0.25% trypsin. Cell pellets were washed with 1× PBS before imaging with a Nikon D50 DSLR camera.

### RNA interference

siRNA was transfected into B16F10 cells using the Lipofectamine RNAi-Max (Invitrogen). After 2 days, cells were harvested and applied for western blot analysis to determine the knockdown efficiency. For cell viability assay, cells were seeded at a density of 1500 cells per well in a 96-well plate. After overnight seeding, the medium in each well was discarded and replaced with fresh medium containing the indicated concentrations of siRNA for 72 h. 10 µL CCK-8 solution (APExBIO, K1018) was then added to each well and incubated for 3 h at 37 °C. The absorbance of each well at 450 nm was read by a microplate reader (PerkinElmer Multimode Plate Reader). The siRNA sequences were listed as below.

	sense (5'-3')	antisense (5'-3')
siMITF	AGCAGUACUUUCUACCA(dT) (dT)	GUGGUAGAAAGGUACUGCU(dT) (dT)
siCtrl	UUUCUCCGAACGUGUCACGU(dT) (dT)	ACGUGACACGUUCGGAGAA(dT) (dT)

### MTT assay

MTT assays were used to assess the viability of different cell lines after incubation with gradient TT-012 or DMSO control. Specifically, cells were seeded into 96-well plates at a density of 1500 cells per well. After

overnight seeding, the medium in each well was discarded and replaced with fresh medium containing gradient TT-012 or DMSO control. After 72 h incubation, 10 µL MTT (Sigma, M2128) solution (5 mg/mL) was added to each well. The cells were then incubated for another 4 h followed by adding 100 µL acidified isopropanol into each well. The plates were further incubated at 37 °C overnight. The absorbance of each well at 560 nm was read by a microplate reader (PerkinElmer Multimode Plate Reader).

### ChIP assay

3x Flag-MITF from mouse MITF melanocyte isoform M (residues 1–419), 3x Flag-MITF<sub>Δ3</sub> from mouse MITF melanocyte isoform M (residues 1–419, removing 264AKD266) and 3x Flag control were cloned into the pcDNA3.1 vector. For transfection, B16F10 cells cultured in 10-cm dish for 24 h were transfected with 10 µg of pcDNA3.1\_3x Flag-MITF, pcDNA3.1\_3x Flag-MITF<sub>Δ3</sub> or control vector using the Lipofectamine 3000 Transfection Reagent (Invitrogen) per the manufacturer's instructions. After 2 days, cells were harvested and applied for western blot analysis to determine the expression level. For ChIP assay, transfected B16F10 cells were treated with TT-012 for 1 h. The cells were rinsed twice with PBS, and the medium was replaced with FBS-free DMEM (GE Healthcare, SH30243.01). B16F10 cells were crosslinked with 0.75% formaldehyde (Sangon Biotech, E672001-0100) for 15 min at room temperature, and the reaction was stopped by adding glycine to a final concentration of 125 mM for 5 min at room temperature. Fixed cells were rinsed twice with ice-cold PBS and resuspended in RIPA buffer containing 50 mM Tris, pH 7.4, 150 mM NaCl, 1% NP-40, and protease inhibitor cocktail (Bimake, B14001). The lysate was sonicated for 15 min (2 s on/6 s off) to shear DNA to an average fragment size of 200–1000 bp. The sample was centrifuged at 14,000 rpm for 10 min. The cleared supernatant was used immediately in ChIP experiments or stored at –80 °C. The sonicated chromatin was incubated with anti-FLAG magnetic beads (Bimake, B26102 or Sigma, M8823) at 4 °C overnight on a vertical roller. The beads were washed for 5 min, once in low salt buffer containing 0.1% SDS, 1% Triton X-100, 2 mM EDTA, pH 8, 20 mM Tris-HCl, pH 8, and 150 mM NaCl, twice in high salt buffer containing 0.1% SDS, 1% Triton X-100, 2 mM EDTA, pH 8, 20 mM Tris-HCl, pH 8, and 500 mM NaCl, twice in LiCl buffer containing 0.25 M LiCl, 1% NP-40, 1% Na deoxycholate, 1 mM EDTA, pH 8, and 10 mM Tris-HCl, pH 8, and once in PBS. After the precipitated material was eluted from anti-FLAG magnetic beads, chromatin was reverse-crosslinked by adding 0.2 M NaCl and incubated at 65 °C for 4 h. DNA levels were quantitatively measured by real-time PCR.

### RNA-Seq analysis

Total RNA was isolated from B16F10 cells treated with 5 µM TT012 or DMSO control for 8 h using a PureLink RNA Mini Kit (Invitrogen). The sequencing was done by the Annaroad Gene Technology (Beijing) Co., Ltd. A total amount of 2 µg RNA per sample was used as input material for the RNA sample preparations. Sequencing libraries were generated using NEBNext® Ultra™ RNA Library Prep Kit for Illumina® (#E7530L, NEB, USA) following the manufacturer's recommendations and index codes were added to attribute sequences to each sample. Briefly, mRNA was purified from total RNA using poly-T oligo-attached magnetic beads. Fragmentation was carried out using divalent cations under elevated temperature in NEBNext First Strand Synthesis Reaction Buffer (5×). First strand cDNA was synthesized using random hexamer primer and RNase H. Second strand cDNA synthesis was subsequently performed using buffer, dNTPs, DNA polymerase I and RNase H. The library fragments were purified with QiaQuick PCR kits and elution with EB buffer, then terminal repair, A-tailing and adapter added were implemented. The aimed products were retrieved and PCR was performed. The clustering of the index-coded samples was performed on a cBot cluster generation system using HiSeq PE Cluster Kit v4-CBot-HS (Illumina) according to the manufacturer's instructions. After cluster generation, the libraries were sequenced on an Illumina platform and 150 bp paired-end reads were generated.

### Murine models of melanoma

Female C57BL/6 mice were obtained from Hunan SJA Laboratory Animal Co., Ltd. (Hunan, China) and were implanted with tumor cells at a proper age (6–8 weeks). All the animals received care in compliance with the guidelines outlined in the Guide for the Care and Use of Laboratory Animals. The procedures were approved by the South China University of Technology Animal Care and Use Committee.

The murine model of melanoma based on the B16F10 mouse melanoma cell line was established by subcutaneous injection of  $5 \times 10^5$  B16F10 cells (diluted in PBS; Matrigel, 9:1 v/v) into the right flank of female C57B/L6 mice.

When the tumor volume reached 50–60 mm<sup>3</sup>, the mice were randomly divided into experimental groups for subsequent experiments. B16F10 melanoma-bearing C57B/L6 mice were treated with TT-012 (2 or 5 mg/kg loaded with PEG-PCL micelles) or vehicle by intravenous tail vein injection every 2 days. The mice were weighed, and tumor volumes were monitored by measuring the perpendicular diameters with a caliper every 2 days during the entire process ( $n = 5$ ). The tumor volumes were calculated with the following formula: tumor volume (mm<sup>3</sup>) = 0.5 × length × width<sup>2</sup>. At the end of the experiment, the treated mice were euthanized and the tumors were excised, photographed and weighed. The cell frequency of major lymphoid and myeloid subsets in the bone marrow, spleen, blood, lymph node and thymus was further analyzed by FACS at the end of treatment to determine the tolerance of TT-012.

A total of  $5 \times 10^5$  B16F10 cells were injected into C57B/L6 cells through the tail vein to establish a melanoma pulmonary metastasis model. Injected mice were randomly divided into 3 experimental groups ( $n = 5$ ) and were treated with TT-012 (2 or 5 mg/kg loaded by PEG-PCL micelles) or vehicle by intravenous tail vein injection every 2 days for 18 days. Mice were euthanized and lung metastatic niches were counted.

### Antibodies for flow cytometry

Lymphocytes of bone marrow, spleen, peripheral blood, lymph nodes and thymus were harvested and isolated. Subsequently, isolated lymphocytes were incubated with Trustain fcXTM (anti-mouse CD16/CD32) to block non-specific binding and then stained with fluorescently labeled monoclonal antibodies against cell surface markers and analyzed on LSRFortessa and FACS Celesta (Becton Dickinson). Dead cells were excluded using DAPI staining analysis. The following antibodies were used: BV786-anti-CD3 (clone 17A2), APC-Cy7-anti-CD4 (clone GK1.5), FITC-anti-CD8a (clone 53-6.7), BV510-anti-CD45 (clone 30-F11), PerCP-Cy5.5-anti-CD19 (clone 6D5), PE-Cy7-anti-B220 (clone RA3-6B2), BV650-anti-CD11b (clone M1/70), PE-anti-F4/80 (BM8), and PerCP-Cy5.5-anti-Ly6c (HK1.4). Data were processed using Flowjo Version 7.61 (TreeStar).

### Toxicity of TT-012 to liver function

C57BL/6 mice were treated with TT-012 for 16 days (2 mg/kg or 5 mg/kg, administered by intravenous tail injection, once every 2 days), or vehicle ( $n = 3$  per group). Then the peripheral blood of treated mice was collected and the levels of GPT and ALP were examined to show liver injury response.

### Patient-derived cancer xenografts

Surgically resected tumor specimens were obtained from patients with histologically confirmed melanoma blinded for age and gender. All surgically resected tumors were collected after written patient consent and in accordance with the ethics committee of Fudan University Shanghai Cancer Center (050432-4-2108). PDX tumors were generated by transplanting small tumor fragments isolated directly from surgical specimens subcutaneously into mice. In each case we first propagated the sample in NPSG mice. After the tumor volume reached 50–100 mm<sup>3</sup>, the mice were randomly grouped. For intravenous tail injection, the mice were treated with TT012 (10 mg/kg or 20 mg/kg loaded with PEG-PCL micelles) or vehicle (PEG-PCL micelles) in the first, third and fifth day every week. For intratumoral injection, the mice were treated with TT012 (20 mg/kg in PBS with 3% DMSO + 1% Tween-80) or PBS (with 3% DMSO + 1% Tween-80) in the first, third and fifth day every week. The tumor volumes were monitored by measuring the perpendicular diameters with a caliper during the entire process. The tumor volumes were calculated with the following formula: tumor volume (mm<sup>3</sup>) = 0.5 × length × width<sup>2</sup>, where length represents the largest tumor diameter and width represents the perpendicular tumor diameter.

### Statistical analysis

The statistical significance in the ChIP experiment was assessed by Student's unpaired *t*-test. The statistical significance of treatment outcomes in animal experiments was assessed by Student's unpaired *t*-test, and one-way ANOVA with Dunnett's correction for multiple pairwise comparisons.

### REFERENCES

- Lo, J. A. & Fisher, D. E. The melanoma revolution: from UV carcinogenesis to a new era in therapeutics. *Science* **346**, 945–949 (2014).
- McGill, G. G. et al. Bcl2 regulation by the melanocyte master regulator Mitf modulates lineage survival and melanoma cell viability. *Cell* **109**, 707–718 (2002).

3. Gray-Schopfer, V., Wellbrock, C. & Marais, R. Melanoma biology and new targeted therapy. *Nature* **445**, 851–857 (2007).
4. Owens, B. Melanoma. *Nature* **515**, S109 (2014).
5. Leclerc, J., Ballotti, R. & Bertolotto, C. Pathways from senescence to melanoma: focus on MITF sumoylation. *Oncogene* **36**, 6659–6667 (2017).
6. Levy, C., Khaled, M. & Fisher, D. E. MITF: master regulator of melanocyte development and melanoma oncogene. *Trends Mol. Med.* **12**, 406–414 (2006).
7. Garraway, L. A. & Sellers, W. R. Lineage dependency and lineage-survival oncogenes in human cancer. *Nat. Rev. Cancer* **6**, 593–602 (2006).
8. Cheli, Y., Ohanna, M., Ballotti, R. & Bertolotto, C. Fifteen-year quest for microphthalmia-associated transcription factor target genes. *Pigment Cell Melanoma Res.* **23**, 27–40 (2010).
9. Garraway, L. A. et al. Integrative genomic analyses identify MITF as a lineage survival oncogene amplified in malignant melanoma. *Nature* **436**, 117–122 (2005).
10. Bertolotto, C. et al. A SUMOylation-defective MITF germline mutation predisposes to melanoma and renal carcinoma. *Nature* **480**, 94–98 (2011).
11. Yokoyama, S. et al. A novel recurrent mutation in MITF predisposes to familial and sporadic melanoma. *Nature* **480**, 99–103 (2011).
12. Johannessen, C. M. et al. A melanocyte lineage program confers resistance to MAP kinase pathway inhibition. *Nature* **504**, 138–142 (2013).
13. Perna, D. et al. BRAF inhibitor resistance mediated by the AKT pathway in an oncogenic BRAF mouse melanoma model. *Proc. Natl. Acad. Sci. USA* **112**, E536–E545 (2015).
14. Haq, R. et al. BCL2A1 is a lineage-specific antiapoptotic melanoma oncogene that confers resistance to BRAF inhibition. *Proc. Natl. Acad. Sci. USA* **110**, 4321–4326 (2013).
15. Cheli, Y. et al. Mitf is the key molecular switch between mouse or human melanoma initiating cells and their differentiated progeny. *Oncogene* **30**, 2307–2318 (2011).
16. Thurber, A. E. et al. Inverse expression states of the BRN2 and MITF transcription factors in melanoma spheres and tumour xenografts regulate the NOTCH pathway. *Oncogene* **30**, 3036–3048 (2011).
17. Goding, C. R. Commentary. A picture of Mitf in melanoma immortality. *Oncogene* **30**, 2304–2306 (2011).
18. McGill, G. G., Haq, R., Nishimura, E. K. & Fisher, D. E. c-Met expression is regulated by Mitf in the melanocyte lineage. *J. Biol. Chem.* **281**, 10365–10373 (2006).
19. Du, J. et al. Critical role of CDK2 for melanoma growth linked to its melanocyte-specific transcriptional regulation by MITF. *Cancer Cell* **6**, 565–576 (2004).
20. Loercher, A. E., Tank, E. M., Delston, R. B. & Harbour, J. W. MITF links differentiation with cell cycle arrest in melanocytes by transcriptional activation of INK4A. *J. Cell Biol.* **168**, 35–40 (2005).
21. Carreira, S. et al. Mitf cooperates with Rb1 and activates p21Cip1 expression to regulate cell cycle progression. *Nature* **433**, 764–769 (2005).
22. Zhu, S. et al. A genomic screen identifies TYRO3 as a MITF regulator in melanoma. *Proc. Natl. Acad. Sci. USA* **106**, 17025–17030 (2009).
23. Zhao, X., Fiske, B., Kawakami, A., Li, J. & Fisher, D. E. Regulation of MITF stability by the USP13 deubiquitinase. *Nat. Commun.* **2**, 414 (2011).
24. Hemesath, T. J. et al. Microphthalmia, a critical factor in melanocyte development, defines a discrete transcription factor family. *Genes Dev.* **8**, 2770–2780 (1994).
25. Pogenberg, V. et al. Restricted leucine zipper dimerization and specificity of DNA recognition of the melanocyte master regulator MITF. *Genes Dev.* **26**, 2647–2658 (2012).
26. Morii, E. et al. Importance of leucine zipper domain of mi transcription factor (MITF) for differentiation of mast cells demonstrated using mi(ce)/mi(ce) mutant mice of which MITF lacks the zipper domain. *Blood* **97**, 2038–2044 (2001).
27. Pogenberg, V. et al. Mechanism of conditional partner selectivity in MITF/TFE family transcription factors with a conserved coiled coil stammer motif. *Nucleic Acids Res.* **48**, 934–948 (2020).
28. Tassabehji, M., Newton, V. E. & Read, A. P. Waardenburg syndrome type 2 caused by mutations in the human microphthalmia (MITF) gene. *Nat. Genet.* **8**, 251–255 (1994).
29. Pingault, V. et al. Review and update of mutations causing Waardenburg syndrome. *Human Mut.* **31**, 391–406 (2010).
30. Wildhardt, G. et al. Spectrum of novel mutations found in Waardenburg syndrome types 1 and 2: implications for molecular genetic diagnostics. *BMJ Open* **3**, e001917 (2013).
31. Grill, C. et al. MITF mutations associated with pigment deficiency syndromes and melanoma have different effects on protein function. *Human Mol. Genet.* **22**, 4357–4367 (2013).
32. Grandori, C., Cowley, S. M., James, L. P. & Eisenman, R. N. The Myc/Max/Mad network and the transcriptional control of cell behavior. *Ann. Rev. Cell Dev. Biol.* **16**, 653–699 (2000).
33. Nair, S. K. & Burley, S. K. X-ray structures of Myc-Max and Mad-Max recognizing DNA. Molecular bases of regulation by proto-oncogenic transcription factors. *Cell* **112**, 193–205 (2003).
34. Landschulz, W. H., Johnson, P. F. & McKnight, S. L. The leucine zipper: a hypothetical structure common to a new class of DNA binding proteins. *Science* **240**, 1759–1764 (1988).
35. Tchan, M. C. & Weiss, A. S. Asn(78) and His(81) form a destabilizing locus within the Max HLH-LZ homodimer. *FEBS Lett.* **509**, 177–180 (2001).
36. Wang, J. et al. Development of an HTS-compatible assay for discovery of melanoma-related microphthalmia transcription factor disruptors using alphaScreen technology. *SLAS Discov.* **22**, 58–66 (2017).
37. Hoek, K. S. et al. Novel MITF targets identified using a two-step DNA microarray strategy. *Pigment Cell Melanoma Res.* **21**, 665–676 (2008).
38. Raja, D. A. et al. pH-controlled histone acetylation amplifies melanocyte differentiation downstream of MITF. *EMBO Rep.* **21**, e48333 (2020).
39. Bianchi-Smiraglia, A. et al. Microphthalmia-associated transcription factor suppresses invasion by reducing intracellular GTP pools. *Oncogene* **36**, 84–96 (2017).
40. Baxter, L. L. & Pavan, W. J. Pmel17 expression is Mitf-dependent and reveals cranial melanoblast migration during murine development. *Gene Expr. Patterns* **3**, 703–707 (2003).
41. Ennen, M. et al. MITF-high and MITF-low cells and a novel subpopulation expressing genes of both cell states contribute to intra- and intertumoral heterogeneity of primary melanoma. *Clin. Cancer Res.* **23**, 7097–7107 (2017).
42. Wu, Q. et al. Microphthalmia-associated transcription factor up-regulates acetylcholinesterase expression during melanogenesis of murine melanoma cells. *J. Biol. Chem.* **293**, 14417–14428 (2018).
43. Ploper, D. et al. MITF drives endolysosomal biogenesis and potentiates Wnt signaling in melanoma cells. *Proc. Natl. Acad. Sci. USA* **112**, E420–E429 (2015).
44. Vaquerizas, J. M., Kummerfeld, S. K., Teichmann, S. A. & Luscombe, N. M. A census of human transcription factors: function, expression and evolution. *Nat. Rev. Genet.* **10**, 252–263 (2009).
45. Bhagwat, A. S. & Vakoc, C. R. Targeting Transcription Factors in Cancer. *Trends Cancer* **1**, 53–65 (2015).
46. Overington, J. P., Al-Lazikani, B. & Hopkins, A. L. How many drug targets are there? *Nat. Rev. Drug Discov.* **5**, 993–996 (2006).
47. Hagenbuchner, J. & Ausserlechner, M. J. Targeting transcription factors by small compounds—Current strategies and future implications. *Biochem. Pharmacol.* **107**, 1–13 (2016).
48. Henchey, L. K., Jochim, A. L. & Arora, P. S. Contemporary strategies for the stabilization of peptides in the alpha-helical conformation. *Curr. Opin. Chem. Biol.* **12**, 692–697 (2008).
49. Fieber, W. et al. Structure, function, and dynamics of the dimerization and DNA-binding domain of oncogenic transcription factor v-Myc. *J. Mol. Biol.* **307**, 1395–1410 (2001).
50. Hoek, K. S. et al. Metastatic potential of melanomas defined by specific gene expression profiles with no BRAF signature. *Pigment Cell Res.* **19**, 290–302 (2006).
51. Arozarena, I. & Wellbrock, C. Targeting invasive properties of melanoma cells. *FEBS J.* **284**, 2148–2162 (2017).
52. Choi, J. et al. Bcl-2 promotes invasion and lung metastasis by inducing matrix metalloproteinase-2. *Cancer Res.* **65**, 5554–5560 (2005).
53. Martina, J. A. & Puertollano, R. Rag GTPases mediate amino acid-dependent recruitment of TFEB and MITF to lysosomes. *J. Cell Biol.* **200**, 475–491 (2013).
54. Ozturk, D. G. et al. MITF-MIR211 axis is a novel autophagy amplifier system during cellular stress. *Autophagy* **15**, 375–390 (2019).
55. Lee, Y. N., Nechushtan, H., Figov, N. & Razin, E. The function of lysyl-tRNA synthetase and Ap4A as signaling regulators of MITF activity in Fc epsilon RI-activated mast cells. *Immunity* **20**, 145–151 (2004).
56. Martina, J. A., Diab, H. I., Li, H. & Puertollano, R. Novel roles for the MiTF/TFE family of transcription factors in organelle biogenesis, nutrient sensing, and energy homeostasis. *Cell. Mol. Life Sci.* **71**, 2483–2497 (2014).
57. Perera, R. M. et al. Transcriptional control of autophagy-lysosome function drives pancreatic cancer metabolism. *Nature* **524**, 361–365 (2015).
58. Davis, I. J. et al. Oncogenic MITF dysregulation in clear cell sarcoma: defining the MiT family of human cancers. *Cancer Cell* **9**, 473–484 (2006).
59. Zhang, W. Z. et al. The protein complex crystallography beamline (BL19U1) at the Shanghai Synchrotron Radiation Facility. *Nucl. Sci. Tech.* **30**, 170 (2019).
60. Collaborative Computational Project, N. The CCP4 suite: programs for protein crystallography. *Acta Crystallogr. D Biol. Crystallogr.* **50**, 760–763 (1994).
61. Emsley, P. & Cowtan, K. Coot: model-building tools for molecular graphics. *Acta Crystallogr. D Biol. Crystallogr.* **60**, 2126–2132 (2004).
62. Adams, P. D., Mustyakimov, M., Afonine, P. V. & Langan, P. Generalized X-ray and neutron crystallographic analysis: more accurate and complete structures for biological macromolecules. *Acta Crystallogr. D Biol. Crystallogr.* **65**, 567–573 (2009).
63. Roehrl, M. H., Wang, J. Y. & Wagner, G. A general framework for development and data analysis of competitive high-throughput screens for small-molecule inhibitors of protein-protein interactions by fluorescence polarization. *Biochemistry* **43**, 16056–16066 (2004).

## ACKNOWLEDGEMENTS

The study is supported by the Lingang Laboratory (LG-QS-202205-11 to J.W. and W.S.); the National Natural Science Foundation of China (21977108 and 21778067 to J.W.; 21778064 and 21977107 to P.F.; and 21621002 to B.Y.); the Shanghai Science and Technology Committee (20511901100 to J.W. and 19411951700 to Y.C.); the Strategic Priority Research Program of the Chinese Academy of Sciences (XDB20000000 to J.W., P.F. and B.Y.); One-hundred Talents Program of Chinese Academy of Sciences (to J.W.); the State Key Laboratory of Bioorganic and Natural Products Chemistry (to J.W., P.F. and B.Y.); a 1000-talent young investigator award (to P.F.); the K. C. Wong Education Foundation (to B.Y.); NIH grants (GM100136 to M.G.; 2P01 CA163222-06; 5R01 AR043369-23; 5R01CA222871-02 and 5R01AR072304-03 to D.E.F.) and the Dr. Miriam and Sheldon G. Adelson Medical Research Foundation (to D.E.F.). The authors also gratefully acknowledge technical supports from Chemical Biology Core Facility at Center for Excellence in Molecular Cell Science, Chinese Academy of Sciences; Fudan University Shanghai Cancer Center Laboratory Animal Science. The authors also grateful acknowledge Prof. Jun Wang for the support on the mice experiments and Dr. Tom Powell and Dr. Tamar Babilla Propp for expert assistance with paper preparation.

## AUTHOR CONTRIBUTIONS

J.W., D.E.F., P.F., M.G., B.Y., and Y.C. provided funding, designed the study, participated in data analysis, drafted and revised the manuscript. Z.L., K.C., J. Dai, P.X., W.S., W.L., Z.Z., S.P.B., P.L., T.M., Y.L., A.K., J.Y., F.W., C.W., M.L., and P.C. designed the study, performed experiments, analyzed the data. P.H., T.P.S., L.S., C.C., L.P., and J.Dong participated in the experiments and/or revised the paper.

## COMPETING INTERESTS

Dr. D.E.F. has a financial interest in Soltego Inc., a company developing SIK inhibitors for topical skin darkening treatments that might be used for a broad set of human applications. Dr. D.E.F. interests were reviewed and are managed by Massachusetts General Hospital and Partners HealthCare in accordance with their competing interests policies.

## ADDITIONAL INFORMATION

**Supplementary information** The online version contains supplementary material available at <https://doi.org/10.1038/s41422-022-00744-5>.

**Correspondence** and requests for materials should be addressed to Yong Chen, Biao Yu, Min Guo, Pengfei Fang, David E. Fisher or Jing Wang.

**Reprints and permission information** is available at <http://www.nature.com/reprints>

Springer Nature or its licensor (e.g. a society or other partner) holds exclusive rights to this article under a publishing agreement with the author(s) or other rightsholder(s); author self-archiving of the accepted manuscript version of this article is solely governed by the terms of such publishing agreement and applicable law.